

2
3 **Pathogenic LRRK2 control of primary cilia and Hedgehog signaling**
4 **in neurons and astrocytes of mouse brain**
5

6 Shahzad S. Khan^{1,3}, Yuriko Sobu^{1,3}, Herschel S. Dhekne¹,
7 Francesca Tonelli^{2,3}, Kerry Berendsen^{2,3}, Dario R. Alessi^{2,3}, and Suzanne R. Pfeffer^{1,3*}
8

9 ¹Department of Biochemistry, Stanford University School of Medicine;

10 ²MRC Protein Phosphorylation and Ubiquitylation Unit, University of Dundee

11 ³Aligning Science Across Parkinson's (ASAP) Collaborative Research Network, Chevy Chase,
12 MD
13

14 *Corresponding Author
15

16 Address:

17 279 Campus Drive

18 Stanford, California, USA 94305-5307
19

20 E-mail Address: pfeffer@stanford.edu
21
22
23
24

Abstract

Activating LRRK2 mutations cause Parkinson's disease, and pathogenic LRRK2 kinase interferes with ciliogenesis. Previously, we showed that cholinergic interneurons of the dorsal striatum lose their cilia in R1441C LRRK2 mutant mice (Dhekne et al., 2018). Here, we show that cilia loss is seen as early as 10 weeks of age in these mice and also in two other mouse strains carrying the most common human G2019S LRRK2 mutation. Loss of the PPM1H phosphatase that is specific for LRRK2-phosphorylated Rab GTPases yields the same cilia loss phenotype seen in mice expressing pathogenic LRRK2 kinase, strongly supporting a connection between Rab GTPase phosphorylation and cilia loss. Moreover, astrocytes throughout the striatum show a ciliation defect in all LRRK2 and PPM1H mutant models examined. Hedgehog signaling requires cilia, and loss of cilia in LRRK2 mutant rodents correlates with dysregulation of Hedgehog signaling as monitored by in situ hybridization of *Gli1* and *Gdnf* transcripts. Dopaminergic neurons of the substantia nigra secrete a Hedgehog signal that is sensed in the striatum to trigger neuroprotection; our data support a model in which LRRK2 and PPM1H mutant mice show altered responses to critical Hedgehog signals in the nigrostriatal pathway.

Introduction

Mutations in the kinase encoded by the LRRK2 gene represent the predominant cause of familial Parkinson's disease (PD), a neurodegenerative disorder that results in the loss of dopaminergic neurons in the substantia nigra pars compacta (Poewe et al. 2017; Alessi and Sammler, 2018). LRRK2 encodes a protein kinase and recent work has shown that a subset of Rab GTPases comprise its primary substrates (Steger et al., 2016; 2017). Pathogenic mutations that localize to LRRK2's ROC domain (eg. R1441C) and kinase domain (eg. G2019S) increase its kinase activity in cells (West et al., 2005; Greggio et al., 2006; Jaleel *et al.*, 2007; Ito *et al.*, 2016; Steger *et al.*, 2016), and interactions with other proteins including Rab29 (Kuwahara et al., 2016; Purlyte et al., 2018; Liu et al., 2018; Gomez et al., 2019) and VPS35 can also activate LRRK2 (Linhart et al., 2014; Mir et al., 2018). Reversal of LRRK2 phosphorylation is mediated at least in part by the PPM1H phosphatase that was recently discovered to specifically reverse LRRK2 action on multiple Rab GTPases (Berndsen et al., 2019). In cell culture, loss of PPM1H in wild type mouse embryonic fibroblast (MEF) cells phenocopies the loss of cilia seen upon expression of pathogenic LRRK2 (Berndsen et al., 2019).

Rab GTPases are master regulators of protein trafficking and carry out their roles by binding to specific partner proteins when the Rabs are GTP-bound (Pfeffer, 2017, 2018). Phosphorylation of Rab proteins interferes with their abilities to be loaded with GTP by cognate guanine nucleotide exchange factors, a prerequisite for their binding to partner effector proteins (Steger et al., 2016, 2017). This alone would interfere with normal Rab GTPase function. Strikingly, once phosphorylated, Rab GTPases switch their preference and bind to new sets of phospho-specific protein effectors. For Rab8 and Rab10 these include RILPL1, RILPL2, JIP3 and JIP4 proteins (Steger et al., 2017; Dhekne et al., 2018; Waschbüsch et al., 2020) and Myosin Va (Dhekne et al., 2021). The consequences of new phospho-Rab interactions include pathways

by which LRRK2 blocks ciliogenesis in cell culture and mouse brain via a process that requires RILPL1 and Rab10 proteins (Steger et al., 2017; Dhekne et al., 2018); centriolar cohesion is also altered (Madero-Pérez et al., 2018; Ordonez et al., 2019).

Although later stages of PD resemble those seen in Alzheimer's disease, PD is first and foremost a movement disorder, and studies to understand its underlying causes must focus on understanding why PD is specifically characterized by dopaminergic neuron loss in the substantia nigra. LRRK2 is most highly expressed in immune cells, lung, kidney and intestine, but it is also present in varying levels throughout the brain (Lis et al., 2018; West et al., 2014; Mandemakers et al., 2012). The striatum is comprised primarily of medium spiny neurons, interneurons and glial cells such as astrocytes. In an important study, Gonzalez-Reyes et al. (2012) showed that dopaminergic neurons in the substantia nigra secrete Sonic Hedgehog (Hh) that is sensed by poorly abundant, cholinergic interneurons in the striatum. Hh is needed for the survival of both these cholinergic target cells and the Hh-producing dopaminergic neurons, despite the fact that only the cholinergic neurons express the PTCH1 Hh receptor. Gonzalez-Reyes et al. (2012) showed further that Hh triggers secretion of glial derived neurotrophic factor (GDNF) from the cholinergic neurons, which provides reciprocal neuroprotection for the dopaminergic neurons of the substantia nigra.

We found previously that the rare, striatal, cholinergic interneurons that would normally sense Hh via their primary cilia are less ciliated in mice carrying the R1441C LRRK2 mutation (Dhekne et al., 2018). In that study, we proposed that cilia loss would decrease the ability of these cells to sense Hh signals. We show here that Hh signaling is indeed impacted by cilia loss in multiple LRRK2 mutant mouse models. Moreover, we show that striatal astrocytes share a broad ciliary deficit that likely impacts synaptic function.

Results

Primary cilia defects in striatal cholinergic interneurons of G2019S LRRK2 mice

We showed previously that cholinergic interneurons that represent about 5% of the neurons in the dorsal striatum of 7-month, R1441C LRRK2 knock-in (KI) mice have fewer primary cilia than their wild type littermates (Dhekne et al., 2018). G2019S LRRK2 is the most common PD-associated mutation in humans, thus it was also important to investigate ciliation in the brains of G2019S LRRK2 mice. G2019S LRRK2 is a hyperactive kinase but less active than R1441C LRRK2 when assayed in cell culture (cf. Steger et al., 2016). The age of the mice was also important: mouse cilia lengthen with age (Arellano et al., 2012) and LRRK2 mutations are incompletely penetrant, making age an important variable in disease onset (Lee et al., 2017; Domingo et al., 2018).

Two different mouse lines were examined: 13-month C57BL/6J mice carrying a genetic knock-in of human LRRK2 G2019S (hereafter referred to as G2019S LRRK2 KI; Steger et al., 2016) and 10-month C57BL/6J mice overexpressing a BAC transgene encoding human G2019S LRRK2 (hereafter referred to as G2019S LRRK2 BAC Tg; Li et al., 2010). Similar to what we observed previously for 7-month R1441C LRRK2 mice, 13-month G2019S LRRK2 KI mice also displayed a significant loss of primary cilia in choline acetyltransferase (ChAT) interneurons of the dorsal striatum (**Figure 1A,B**). As before, primary cilia loss was cell-type specific as there was no difference in ciliation or cilia length in the surrounding cells (primarily medium spiny neurons) between mutant and wild type groups (**Figure 1–figure supplement 1**). For cholinergic neurons that retained cilia, we detected no significant difference in length between wild type and mutant groups (**Figure 1C**). Cilia length is important to assess as it is thought to reflect signaling capacity (Guo et al., 2017).

G2019S LRRK2 BAC Tg mice overexpress LRRK2 protein by approximately six-fold (Li et al., 2010) and might be expected to display a more severe phenotype than the G2019S LRRK2 KI mice. In the brains of the 10-month G2019S LRRK2 BAC Tg mice we also detected a decrease in ciliated cholinergic interneurons (**Figure 1D,E**), comparable to that seen in the G2019S KI mice; when a primary cilium was present, it was not significantly shorter than wild type control cells (**Figure 1F**); again, there was no change in ciliation for the surrounding neurons. Taken together, these data show that G2019S LRRK2 mice have primary cilia defects of the same magnitude as previously observed in cholinergic neurons of the dorsal striatum of R1441C LRRK2 KI mice and cultured cells (Steger et al., 2017; Dhekne et al., 2018). Unlike the R1441C mice however, G2019S mice did not show defects in cortical ciliogenesis (**Figure 1-Figure Supplement 1**).

Ciliary defects in G2019S Striatal Astrocytes

Mouse LRRK2 is more highly expressed in astrocytes than neurons (Zhang et al., 2014; <http://www.brainrnaseq.org>), thus it was important to explore the consequences of LRRK2 mutation on mouse astrocyte ciliation. We used glial fibrillary acidic protein (GFAP) and S100 Calcium Binding Protein B (S100B) to identify astrocytes in the striatum. Astrocytic primary cilia were detected using antibodies specific for ADP Ribosylation Factor Like GTPase 13B (Arl13B) because astrocytes in adult mouse brain do not express detectable amounts of Adenylate Cyclase 3 that we use to stain cilia in neurons (Dhekne et al. 2018; Sterpka and Chen, 2018; Sipos et al., 2018; Kasahara et al., 2014).

Strikingly, we found that GFAP⁺ G2019S LRRK2 KI and G2019S BAC Tg astrocytes in the dorsal striatum were less likely to have Arl13B⁺ primary cilia relative to wild type controls (**Figure 2**). In addition, the remaining GFAP⁺ cilia in the G2019S BAC Tg astrocytes were very slightly but significantly shorter (**Figure 2F**). Thus, GFAP⁺ striatal astrocytes from G2019S

LRRK2 KI mice have fewer primary cilia, and striatal astrocytes also have shorter primary cilia upon pathogenic LRRK2 overexpression. Note that astrocyte cilia were shorter overall compared with neuronal cilia (**Figures 1C,F and 2C,F**), and all cilia were shorter in the BAC Tg mice.

As shown in **Figure 3A,B**, primary cilia loss in cholinergic interneurons of the dorsal striatum could be detected as early as 10 weeks of age in R1441C LRRK2 KI mice; note that these were the youngest animals analyzed. At this age, fewer striatal cholinergic interneurons have a primary cilium (~40%) in comparison with their non-transgenic littermates (~60%; **Figure 3B**). Overall neuronal ciliation in the dorsal striatum in 10-week wild type and R1441C mutant groups was slightly lower but similar to the overall values seen previously in a 7-month R1441C LRRK2 KI cohort (~70%; Dhekne et al 2018).

MLi-2 treatment failed to reverse cilia loss in young R1441C LRRK2 KI mice

LRRK2 kinase inhibitors are of great interest due to their potential to normalize LRRK2 kinase activity in patients carrying hyperactive LRRK2 mutant forms. Moreover, if ciliation is a relevant disease phenotype, it would be important to know if cilia defects can be corrected in mutant mice treated with a LRRK2 inhibitor. R1441C LRRK2 KI mice were fed the LRRK2 inhibitor, MLi-2, for two-weeks for phenotypic analysis.

As shown in **Figure 3A,C,D**, two weeks of MLi-2 feeding did not alter the extent of ciliation or cilia length in cholinergic interneurons or astrocytes in the LRRK2 R1441C mice. We also scored primary cilia in two distinct populations of astrocytes – cells that were positive for both GFAP and S100B, and those that were only positive for S100B (**Figure 3E-G**). Despite two weeks of MLi-2 administration, we failed to detect a significant difference in ciliation or cilia length for either population of astrocytes upon treatment. It is important to note that neurons

and astrocytes are postmitotic cells with much less dynamic cilia than dividing cells (Sterpka and Chen, 2018); longer times of drug treatment may very well be needed to reveal an effect.

The ability of MLi-2 to block LRRK2-mediated Rab10 phosphorylation in whole, R1441C LRRK2 mutant mouse brains was assessed by western blot (**Figure 4A,B**). LRRK2 inhibitors decrease LRRK2 phosphorylation at serine 935 (cf. Fell et al., 2015), and pS935-LRRK2 was diminished in wild type and R1441C LRRK2 brains from mice fed MLi-2 inhibitor, consistent with inhibitor access in this tissue. Rab12 S105 phosphorylation also decreased in wild type (**Figure 4C**) and mutant (**Figure 4A,B**) brain. However, levels of pRab10 seemed unchanged (**Figure 4A,B**) with variability among animals (see also Ianotta et al., 2020). Previous studies have also noted that MLi-2 administration does not markedly reduce pRab10 levels in brain (Kelly et al., 2018; Kalogeropoulou et al., 2020; Nirujogi et al., 2021; Kluss et al., 2021). Note that analysis of whole brain in this experiment will not capture the precise status of pRab10 levels in rare cholinergic neurons of the dorsal striatum that show LRRK2 mutation-associated ciliary deficits. Unfortunately the available anti-phosphoRab10 antibody cannot be used for tissue immunohistochemistry at a single cell level.

PPM1H deficiency phenocopies LRRK2 mutation

PPM1H phosphatase specifically dephosphorylates LRRK2 Rab GTPase substrates (Berndsen et al., 2019). If LRRK2 action is responsible for loss of cilia in mutant mouse brains, loss of the corresponding phosphatase should yield the same phenotype in that tissue. **Figure 5** shows that even heterozygous loss of PPM1H leads to decreased cilia numbers in cholinergic interneurons (**Figure 5A,B**) and astrocytes (**Figure 5C,D**) of the dorsal striatum of 5.5 month old mice. Analysis of 2.5 month old homozygous PPM1H knockout mice showed a slightly greater defect, despite the fact that fewer cholinergic neurons were ciliated at this age (compare Fig. 5B left and right panels). These data demonstrate the importance of high PPM1H levels in wild

type brain to counteract LRRK2 action. More importantly, they strongly validate a link between LRRK2-Rab phosphorylation and ciliogenesis in specific brain cell types because loss of the phosphatase shows the same phenotype as the presence of a hyperactive LRRK2 mutation. Immunoblotting showed an appropriate reduction of PPMH protein levels in brain extracts from *Ppm1h^{+/-}* and *Ppm1h^{-/-}* mice, with levels of pRab10 barely changed at least for whole brain tissue from the heterozygous knockout animals with a greater increase for the *Ppm1h^{-/-}* animals (Fig. 5-Figure Supplement 1).

Sonic hedgehog signaling is altered in mutant LRRK2 mice

Although Hh signaling is critical during neuronal development, little is known about Hh signaling in the adult brain. As mentioned earlier, striatal ChAT⁺ interneurons respond to Sonic hedgehog ligands that originate from dopaminergic neurons in the substantia nigra. Sonic hedgehog signaling requires cilia: the transmembrane transducer Smoothened must translocate to the primary cilium to initiate the signaling cascade that results in the expression of the transcription factor *Gli1*, a direct Hh target gene that serves as a widely-used metric for signaling strength (Corbit et al, 2005; Rohatgi et al, 2007). Thus, primary ciliogenesis is likely critical for proper Hh sensing. We thus examined Hh signaling in LRRK2 mutant animals with pathogenic LRRK2 mutations and associated ciliary defects.

Gli1 transcripts were detected in brain slices using the RNAscope method of fluorescence *in situ* hybridization. **Figure 6A** shows detection of *Gli1* transcripts in wild type, ChAT⁺ neurons, which appear as white dots; a negative control hybridization probe yielded no signal under parallel conditions (**Figure 6A**, bottom row). As expected, ciliated ChAT⁺ neurons showed higher levels of *Gli1* transcripts compared with non-ciliated cells in both mutant and wild type mice (**Figure 6D**). Ciliated cholinergic neurons also displayed the highest number of *Gli1* positive dots compared with all other cell types in the striatum (monitored by DAPI staining) and compared

with non-ciliated cholinergic neurons (**Figure 6C,D**). This matches well with prior estimates that expression of the Hh receptor PTCH1 is restricted to 6% of total striatal neurons representing all cholinergic and fast spiking interneurons (Gonzalez-Reyes et al., 2012).

Importantly, the number of *Gli1* dots trended higher in ciliated, striatal cholinergic interneurons of R1441C LRRK2 mice (3-4 *Gli1* positive dots) compared with wild type mice (**Figure 6D,E**). Taken together, these data show that although overall ciliation is decreased, the remaining, ciliated, striatal cholinergic interneurons in R1441C LRRK2 mice transcribe higher quantities of *Gli1* in response to R1441C LRRK2 expression. The upregulation of *Gli1* transcripts in the remaining ciliated neurons could be due to increased Hh production in the substantia nigra; perhaps the overall decrease in ciliation decreases GDNF production in the striatum, increasing Hh production by subsequently stressed, dopaminergic neurons. Alternatively, the remaining cilia in LRRK2 mutant brains may be structurally intact but functionally altered, leading to increased *Gli1* transcript levels. Finally, these data also reveal highly localized Hh signaling in cholinergic neurons in the dorsal striatum compared with their surrounding neighbors, as predicted by the distribution of PTCH1 protein (Gonzalez-Reyes et al., 2012).

Because R1441C LRRK2 striatal astrocytes also have fewer cilia, we determined if their ability to sense or respond to Hh was also altered. Astrocytes express higher levels of PTCH1 receptor than neurons in both rodent and human brain, and thus would be expected to be capable of Hh signaling. **Figure 7A,B** shows astrocytic *Gli1* detection using RNAscope; two classes of astrocytes were scored: those expressing S100B or GFAP. Consistent with the requirement for cilia for canonical Hh signaling, ciliated astrocytes had more *Gli1* dots than non-ciliated astrocytes, independent of whether or not the cells expressed pathogenic R1441C LRRK2 (**Figure 7C,D**): in contrast to ChAT⁺ interneurons (**Figure 6**), ciliated and non-ciliated striatal astrocytes from R1441C LRRK2 had similar numbers of *Gli1* positive dots relative to their

ciliated wild type controls. Altogether, these data show that striatal astrocytes respond to Hh signaling similarly in R1441C LRRK2 and wild type mice on an individual cell basis, but overall loss of ciliation due to the LRRK2 mutation appears to lead to an overall decreased striatal astrocytic response.

We next explored if pathogenic LRRK2-associated cilia deficits impact GDNF production by cholinergic neurons of the dorsal striatum. RNAscope fluorescence in situ hybridization for *Gdnf* transcripts showed that most GDNF was expressed by cholinergic neurons (and not surrounding cells) in the dorsal striatum of wild type mice, consistent with previous reports (Hidalgo-Figueroa et al., 2012; **Figure 8**). Moreover, *Gdnf* RNA was preferentially detected in ciliated wild type cells, consistent with induction by a cilia-mediated pathway such as the Hedgehog pathway (**Figure 8A, C**). From this result, we anticipated that the increased proportion of non-ciliated cells in LRRK2 mutant animals would lead to an overall deficit in *Gdnf* transcription. Quantitation of total *Gdnf* transcripts failed to detect a significant decrease in overall *Gdnf* transcript signal in 5.5 month old LRRK2 G2019S mice compared with wild type animals, under conditions in which we detected an ~40% loss of primary cilia (**Fig. 8C**). Gonzalez-Reyes et al. (2012) noted a strong age dependence for loss of GDNF production in the absence of Hh signaling; it is possible that older (12 month old) mice will show a greater defect in *Gdnf* transcript production. Also note that transcript levels may not correlate with protein production.

An completely unexpected result was obtained when we determined the relative contribution of ciliated and non-ciliated neurons in G2019S mutant dorsal striatum to overall *Gdnf* transcript production (**Fig. 8D**). Unlike their wild type counterparts, non-ciliated cholinergic neurons in LRRK2 G2019S striatal sections showed significantly higher levels of *Gdnf* gene expression, consistent with Hedgehog signaling dysregulation. The Hedgehog signaling pathway triggers *cilia-dependent* processing of the Gli3 protein: Gli3 can be converted into a transcriptional

activator or it can be converted into a transcriptional repressor (Bangs and Anderson, 2017; Kong et al., 2019). It is possible that loss of Gli3 repression in non-ciliated LRRK2 mutant neurons increases GDNF production in those cells. Indeed, recent CHIP-Seq experiments identify the *Gdnf* gene as a Gli3-binding region, at least in the developing mouse limb bud (Lex et al., 2020). Finally, GDNF represses Sonic Hedgehog production by dopaminergic neurons (Gonzalez-Reyes et al., 2012); this may explain the decrease in *Gdnf* transcripts in ciliated LRRK2 mutant cholinergic neurons relative to wild type animals, in response to the increased GDNF production by neighboring, non-ciliated LRRK2 mutant cholinergic neurons. Similar analysis of the relative contribution of ciliated cells to *Gli1* transcription in R1441C striatum (as in Fig. 6) was consistent with a similar trend of dysregulation in unciliated mutant neurons (Fig. 8D). Future experiments will seek to isolate these cells for single cell transcriptomic and/or proteomic analyses to determine the underlying basis for the differences observed for Hedgehog pathway components between ciliated and nonciliated mutant neurons.

Phosphorylated Rab10 in astrocyte ciliogenesis

Our previous work in mouse embryonic fibroblasts and patient-derived iPS cells showed the importance of LRRK2-phosphorylated Rab10 and its effector, RILPL1 in primary ciliogenesis blockade (Dhekne et al., 2018). In addition, the fact that PPM1H mutant animals phenocopy hyperactive LRRK2 kinase mutants strongly implicates Rab GTPase phosphorylation in the phenotypes observed. Unfortunately it was not possible to detect pRab10 directly in mouse brain sections. To explore further the possible contribution of pRab10 to ciliogenesis blockade in astrocytes, we used immunopanning methods (Foo et al., 2011) to obtain primary, poorly dividing astrocytes from G2019S^{+/-} LRRK2 rat brains. Cells are grown in defined, serum-free media containing 5ng/ml soluble heparin binding EGF-like growth factor (HbEGF) that activates the EGF receptor (Citri and Yarden, 2006) and acts via the EGF receptor in these cells (Foo et

al., 2011). Cell density is also relevant as cultured astrocytes secrete other autocrine trophic factors, and ciliogenesis is enhanced in cell culture by increased cell density.

G2019S^{+/-} panned astrocytes showed ~ 60% ciliation when grown under sparse conditions (**Figure 9A,B**) as monitored using anti-Arl13B antibodies. Similar to what we have detected in multiple cell types in culture (Steger et al., 2017; Dhekne et al., 2018), pRab10 levels were highest in non-ciliated cells in the absence of the MLI-2 LRRK2 inhibitor (**Figure 9B**), consistent with a correlation between pRab10 and ciliogenesis.

Discussion

Pathogenic LRRK2 activity causes primary cilia loss in striatal cholinergic interneurons in mature R1441C LRRK2 mice (Dhekne et al., 2018). In this study, we show that primary cilia loss is also seen in two distinct G2019S LRRK2 mouse models of the most common human LRRK2 mutation. Moreover, our study reveals that primary cilia loss in cholinergic interneurons can be detected as early as 10 weeks of age, the youngest age we examined. Thus, pathogenic LRRK2 activity causes interneuron primary cilia loss at a relatively early stage and loss is sustained throughout the animal's lifespan for post-mitotic neurons. Consistent with this conclusion was our finding that mice deficient in the phospho-Rab-specific phosphatase, PPM1H, show the same ciliary defect as mice harboring a pathogenic LRRK2 mutation. This provides strong genetic evidence for the importance of LRRK2 activity in regulating cilia formation, in both LRRK2 wild type/PPM1H deficient and LRRK2 mutant animals.

Striatal cholinergic interneurons provide trophic support to dopaminergic neurons via Hh sensing (Gonzalez-Reyes et al., 2012), and primary cilia loss is predicted to perturb the ability of cholinergic neurons to sense Hh ligands as required for this role. Our FISH results support this model by showing that ciliated striatal ChAT⁺ interneurons express *Gli1* transcripts under

normal, physiologic conditions, and represent the cell type showing the greatest level of *Gli1* expression in the dorsal striatum. In the presence of the pathogenic R1441C LRRK2 mutation, we observed significant elevation of *Gli1* transcripts in the smaller number of remaining, ciliated, striatal cholinergic interneurons. One explanation for this increase in *Gli1* mRNA is that dopaminergic neurons in the substantia nigra upregulate Hh production due to stress or lack of GDNF signals from the striatum. Cortical neurons have been shown by others to require primary cilia to protect against stresses of ethanol- or ketamine-induced caspase activation and dendritic degeneration (Ishii et al., 2021). Future experiments will seek to monitor changes in Hh production in the substantia nigra that may be associated with LRRK2 mutation.

It was previously reported that loss of Hedgehog production by dopaminergic neurons decreases *Gdnf* transcripts and protein levels in the striatum in an age-dependent manner, with a ten fold mRNA decrease seen between 1 and 12 months and a 35% decrease in GDNF protein at 4 months of age (Gonzalez-Reyes et al., 2012). These authors assayed the entire striatum; it is important to note that significant GDNF is produced in the ventral striatum (Barroso-Chinea et al., 2005) and may account for some portion of the changes those authors observed. In our single cell analyses of cells in the dorsal striatum, we did not detect a significant decrease in *Gdnf* transcripts at 5 months age in LRRK2 G2019S striatal cholinergic neurons compared with age matched, wild type controls. It will be important for us to analyze older mice as these showed a more significant change in the prior study, and to try to carry out GDNF protein analysis specifically in the dorsal striatum.

While transcription of the Hh target genes, *Gli1* and *Gdnf* were entirely cilia-dependent in wild type cholinergic neurons, this selectivity was lost in G2019S and R1441C animals, where unciliated cells showed a much higher contribution to total *Gli1* and *Gdnf* transcript levels. Both of these genes are Gli3 repressor targets and one would have expected that the absence of a

cilium would resemble a condition in which Gli3 repressor is high and target gene expression low. Future work will seek to clarify this unexpected dysregulation of the Hh signaling pathway.

L-dopa induced dyskinesia is a debilitating side effect of dopamine replacement therapy for Parkinson's disease. Malave et al. (2021) have shown that Smoothed activation in striatal cholinergic neurons protects mice from L-dopa induced dyskinesia. These experiments highlight the importance of the Hedgehog signaling pathway for movement coordination regulated by the nigrostriatal circuit, and underscore the importance of studying the consequences of cilia loss associated with LRRK2 mutations since cilia are critical for Hedgehog signaling.

Loss of Cilia in Astrocytes

For the first time we show that LRRK2 G2019S striatal astrocytes are also cilia-deficient at 5.5-13 months of age and Gli levels correlated with the presence of primary cilia. The data indicate that fewer striatal astrocytes in LRRK2 G2019S mice are capable of responding to Hh ligands and importantly, the remaining astrocytes that do respond do not compensate for general loss in ciliated cells. How might decreased Hh sensing by astrocytes impact the striatum? Striatal astrocytes functionally interact with distinct networks of medium spiny neurons (Khakh, 2019; Martín et al., 2015), and loss of Hh sensing may perturb these interactions. This is relevant because imbalances in medium spiny neuron activity are known to contribute to the slowness and rigidity of movement that is symptomatic of Parkinson's disease (Zhai et al., 2018).

Chen et al. (2020) recently reported altered organization of glutaminergic AMPA receptors in cultured striatal neurons from LRRK2 G2019S and R1441C mutant mice. This was accompanied by decreased frequency of miniature excitatory post-synaptic currents in brain slices. It is likely that LRRK2-mediated Rab phosphorylation is in some way responsible for

these changes; Rab phosphorylation could of course regulate the trafficking of AMPA receptors. It is also possible that in the brain, overall physiological changes are due to loss of cilia from the astrocytes that surround these neurons and support their overall physiology.

Decreased Hh signaling in astrocytes results in the reduction of Kir4.1 potassium channel expression in the cerebellum and neocortex and impairs turnover of dendritic spines, accompanied by an increase in neuronal excitability (Farmer et al., 2016; Hill et al., 2019). Kir4.1 expression is markedly decreased in several neurological disorders (cf. Scholl et al., 2009; Inyushin et al., 2010; Gilliam et al., 2014), including in striatal cells of Huntington's disease mice (Tong et al., 2014; Dvorzhak et al., 2016). Striatal astrocytes may use Kir4.1 channels to modulate medium spiny neuron synaptic transmission by local buffering of potassium ions, as was shown for other brain regions (Djukic et al., 2007, Sibille et al., 2014). Thus, primary cilia loss from LRRK2 G2019S striatal astrocytes is likely to influence medium spinal neuron circuitry.

Two weeks of LRRK2 MLi-2 inhibitor administration failed to reverse cilia deficits in LRRK2 mutant animals. This may not be surprising as cilia are likely long lived in post-mitotic neurons and non-reactive astrocytes. Very little is known about the dynamics of cilia in the adult brain, however data from experiments in which a critical ciliary component, IFT88 was inducibly knocked out in adult brain indicated that 3 months was needed to see the consequences of loss of this ciliary factor (Bowie and Goetz, 2020). Thus, it is possible that longer feeding regimens will reveal a recovery in striatal ciliation. Another puzzle is why pRab10 levels do not change as significantly as pRab12 and LRRK2 pS935 in immunoblots of whole brains of drug treated animals. It is possible that in the brain, pRab10 is greatly stabilized by strong effector binding. It is important to remember that levels of pRab10 in the very small population of cholinergic neurons of the dorsal striatum may be of major consequence for Hedgehog signaling in the

nigrostriatal circuit and MLI-2 sensitivity of pRab10 in these cells would be missed in whole brain immunoblots.

Altogether, these data demonstrate a profound effect of LRRK2 hyperactivation on primary ciliogenesis in a population of cholinergic interneurons that play a key role in motor function and in astrocytes that support medium spiny neuron function in the dorsal striatum. Dysregulation of Hedgehog signaling by cholinergic interneurons and astrocytes of the striatum may contribute to the loss of dopaminergic neurons associated with a disease of aging such as Parkinson's disease.

Acknowledgements

This study was funded by the joint efforts of The Michael J. Fox Foundation for Parkinson's Research (MJFF) [17298 & 6986 (S.R. P. & D.R.A.)] and Aligning Science Across Parkinson's (ASAP) initiative. MJFF administers the grant (ASAP-000463, S.R.P. & D.R.A.) on behalf of ASAP and itself. Funds were also provided by the Medical Research Council [grant no. MC_UU_12016/2 (D.R.A.)] and the pharmaceutical companies supporting the Division of Signal Transduction Therapy Unit (Boehringer-Ingelheim, GlaxoSmithKline, Merck KGaA (D.R.A.)).

For the purpose of open access, the authors have applied a CC-BY public copyright license to the Author Accepted Manuscript version arising from this submission. All primary data associated with each figure has been deposited in the Dryad repository and can be found at <https://doi.org/10.5061/dryad.76hdr7sxx>. We are especially grateful to Drs. Rajat Rohatgi and Jennifer Kong for their critical input and Dr. Andreas Kottman for helpful discussion.

Materials and Methods

Reagents: MLI-2 LRRK2 inhibitor was synthesized by Natalia Shpiro (MRC Reagents and Services, University of Dundee) and was first described to be a selective LRRK2 inhibitor in previous work (Fell et al., 2015).

Transgenic Mice: All animal studies were performed in accordance with the Animals (Scientific Procedures) Act of 1986 and regulations set by the University of Dundee, the U.K. Home Office, and the Administrative Panel on Laboratory Animal Care at Stanford University. Mice were maintained under specific pathogen-free conditions at the University of Dundee (U.K.); they were multiply housed at an ambient temperature (20–24°C) and humidity (45–55%) and maintained on a 12 hr light/12 h dark cycle, with rodent diet and water available ad libitum. LRRK2 R1441C knock-in mice backcrossed on a C57BL/6J background, were obtained from the Jackson laboratory (Stock number: 009346). LRRK2 G2019S knock-in and PPM1H knock-out mice backcrossed on a C57BL/6J background, were obtained from Taconic (Model 13940 and TF3142, respectively). G2019S BAC transgenic brain sections from 10-month mice were a gift from Aaron Gitler at Stanford (Li et al., 2010). Mouse genotyping was performed by PCR using genomic DNA isolated from tail clips or ear biopsies. For the experiment shown in Figure 5-Figure Supp. 1, 63-83 day old mice of the indicated genotypes were injected subcutaneously with vehicle [40% (w/v) (2-hydroxypropyl)- β -cyclodextrin (Sigma–Aldrich #332607)] or MLI-2 dissolved in the vehicle at a 30 mg/kg final dose. Mice were euthanized by cervical dislocation 2hr following treatment and the collected tissues were rapidly snap frozen in liquid nitrogen.

Mouse brain processing: Homozygous LRRK2-mutant (R1441C or G2019S of various ages as indicated) or heterozygous *Ppm1h*^{+/+} mice (164 days old) and age-matched wild-type controls were fixed by transcardial perfusion using 4% paraformaldehyde (PFA) in PBS as described in Khan et al. (2020). Next, whole brain tissue was extracted, post-fixed in 4% PFA for 24 hrs and

454 then immersed in 30% (w/v) sucrose in PBS until the tissue settled to the bottom of the tube
455 (~48 hrs). LRRK2 R1441C KI, LRRK2 G2019S KI and *Ppm1h*^{-/+} brains were harvested in
456 Dundee and sent with identities blinded until analysis was completed. Prior to cryosectioning,
457 brains were embedded in cubed-shaped plastic blocks with OCT (BioTek, USA) and stored at
458 -80°C. OCT blocks were allowed to reach -20°C for ease of sectioning. The brains were
459 oriented to cut sagittal or coronal sections on a cryotome (Leica CM3050S, Germany) at 16-25
460 µm thickness and positioned onto SuperFrost plus tissue slides (Thermo Fisher, USA).

461

462 *In-diet MLI-2 administration to wild-type mice (pilot study) and LRRK2 R1441C KI mice:* For the
463 experiment shown in Figure 4, 11 C57BL/6j wild-type mice were allowed to acclimate to the
464 control rodent diet (Research Diets D01060501; Research Diets, New Brunswick, NJ) for 14
465 days before being placed on study. On day 1 of the study, one group (4 mice) received modified
466 rodent diet (Research Diets D01060501) containing MLI-2 and formulated by Research Diets to
467 provide a concentration of 60 mg/kg per day on the basis of an average food intake of 5 g/day
468 for 14 days; the other group (7 mice) received untreated diet (Research Diets D01060501) for
469 14 days and served as the control group. The dose of MLI-2 and the length of the in-diet
470 treatment used for this study were based on Fell et al., 2015. Bodyweight and food intake were
471 assessed twice weekly. On the last day of the study, 3 mice from the control diet group received
472 30mg/kg MLI-2 dissolved in 40% (w/v) (2-hydroxypropyl)- β-cyclodextrin via subcutaneous
473 injection for 2 hr prior to tissue collection. All mice were euthanized by cervical dislocation and
474 the collected tissues were rapidly snap frozen in liquid nitrogen and brain samples used for
475 quantitative immunoblotting analysis of phospho-Ser935 LRRK2 and phospho-Ser105 Rab12 as
476 a readout of LRRK2 activity.

477 For the experiments described in Figure 3C-G, littermate or age-matched male and female
478 LRRK2 R1441C homozygous knock-in mice at 10 weeks of age were used. Mice were allowed
479 to acclimate to the control rodent diet for 14 days as described above before being placed on
480 study. On day 1 of the study, one group (7 mice) received a modified rodent diet targeted to
481 provide a concentration of 60 mg/kg per day on the basis of an average food intake of 5 g/day;
482 the other group (7 mice) received an untreated diet and served as the control group.
483 Bodyweight and food intake were assessed twice weekly. On day 15, mice were terminally
484 anesthetized and brains harvested and fixed as described above. For immunoblotting analysis
485 to confirm LRRK2 inhibition, brains were snap frozen in liquid nitrogen from mice that were
486 terminally anesthetized and perfused by injection of PBS into the left cardiac ventricle (2 mice
487 from each group).

488 *Preparation of mouse tissue lysates for immunoblotting analysis:* Snap frozen tissues were
489 weighed and quickly thawed on ice in a 10-fold volume excess of ice-cold lysis buffer containing
490 50 mM Tris-HCl pH 7.4, 1 mM EGTA, 10 mM 2-glycerophosphate, 50 mM sodium fluoride, 5
491 mM sodium pyrophosphate, 270 mM sucrose, supplemented with 1 µg/ml microcystin-LR, 1 mM
492 sodium orthovanadate, complete EDTA-free protease inhibitor cocktail (Roche), and 1% (v/v)
493 Triton X-100. Tissues were homogenized using a POLYTRON homogenizer (KINEMATICA),
494 employing three rounds of 10 s homogenization with 10 s intervals on ice. Lysates were clarified
495 by centrifugation at 20 800g for 30 min at 4°C and supernatant was collected for subsequent
496 protein quantification by Bradford assay and immunoblot analysis.

497 *Quantitative immunoblotting analysis:* 40 µg of brain extracts were loaded onto a NuPAGE 4–
498 12% Bis-Tris Midi Gel (Thermo Fisher Scientific, Cat# WG1402BOX) and electrophoresed at
499 130 V for 2 hrs with NuPAGE MOPS SDS running buffer (Thermo Fisher Scientific, Cat#
500 NP0001-02). Proteins were then electrophoretically transferred onto a nitrocellulose membrane
501 (GE Healthcare, Amersham Protran Supported 0.45 µm NC) at 100 V for 90 min on ice in

transfer buffer (48 mM Tris–HCl and 39 mM glycine supplemented with 20% (v/v) methanol). The transferred membrane was blocked with 5% (w/v) skim milk powder dissolved in TBS-T (50 mM Tris base, 150 mM sodium chloride (NaCl), 0.1% (v/v) Tween 20) at room temperature (RT) for 30 min and incubated overnight at 4°C in primary antibodies diluted in 5% (w/v) BSA in TBS-T. After incubation with primary antibodies, membranes were washed three times for 5 min with TBS-T and incubated with near-infrared fluorescent dye-labelled secondary antibodies (diluted to 1:20,000) for 1 hr at RT. Thereafter, membranes were extensively washed with TBS-T and protein bands were acquired via near-infrared fluorescent detection using the Odyssey CLx imaging system and the signal intensity quantified using Image Studio software.

Fluorescence in situ hybridization (FISH)

Wild type (WT) and R1441C LRRK2 KI 10-month mouse brains were sliced coronally at 25 µm thickness. RNAscope® Multiplex Fluorescent Detection Kit v2 (Advanced Cell Diagnostics) was carried out according to the manufacturer using RNAscope® 3-plex Negative Control Probe (#320871) or Mm-*Gli1* (#311001). Opal 690 (Akoya Biosciences) was used for fluorescent visualization of hybridized probes. Then, brain slices were blocked with 0.1% BSA and 10% donkey serum in TBS (Tris buffered saline) containing 0.1% Triton X-100 for 30 mins followed by incubation with primary antibody in TBS + 0.1% BSA and 1% DMSO overnight at 4 °C. Secondary antibody was also diluted in TBS + 0.1% BSA and 1% Triton X-100 for 30 mins and then added for 2 hrs at RT. Sections were mounted with ProLong™ Gold Antifade Mountant with DAPI and glass coverslips. For *Gdnf* RNA experiments, WT and G2019S LRRK2 KI 5-month mouse sections were sliced coronally at 25 µm thickness. RNAscope® Multiplex Fluorescent Detection was performed as above using Mm *Gdnf* (#421951) diluted 1:10 in dilution buffer (6x saline-sodium citrate buffer (SSC), 0.2% lithium dodecylsulfate (Research Products International; #RPI-L26200), and 20% Calbiochem® OmniPur® Formamide (#75-12-7)).

Immunofluorescence staining and microscopy: Brain primary cilia detection and analyses were performed as previously described (Khan et al., 2020). Briefly, frozen slides were thawed at RT for 10 min then gently washed with PBS for 5 min. Sections were permeabilized with 0.1% Triton X-100 in PBS at RT for 15 min. Sections were blocked with 2% BSA in PBS for 2 hrs at RT and were then incubated overnight at 4°C with primary antibodies. The following day, sections were incubated with secondary antibodies at RT for 2 hr. Donkey Highly cross absorbed H + L secondary antibodies (Life Technologies) conjugated to Alexa 488, Alexa 568 or Alexa 647 were used at a 1:1000 dilution. Stained tissues were overlayed with Mowiol and a glass coverslip. All antibody dilutions for tissue staining included 1% DMSO to help antibody penetration. All images were obtained using a spinning disk confocal microscope (Yokogawa) with an electron multiplying charge coupled device (EMCCD) camera (Andor, UK) and a 100X 1.4 NA oil immersion objective. All image visualizations and analyses were performed using Fiji (RRID:SCR_002285; Rueden et al., 2017). Cholinergic neurons in the dorsal striatal region were identified in the caudate putamen of sagittal or coronal sections that were reactive for both choline acetyltransferase and the pan neuronal marker, NeuN. Dorsal striatal astrocytes were defined as GFAP⁺ and/or S100B⁺ cells in the caudate putamen.

Astrocyte Immune-Panning and Microscopy: Rat Astrocyte Immune-panning was performed as previously described (Foo et al., 2013; Dhekne et al., 2018). Cells on coverslips were fixed with 3.5% PFA for 15 minutes at RT. The cells were then subjected to three washes with PBS for 5 min each. To permeabilize, samples were incubated with PBS containing 0.1% Saponin for 15 min. All subsequent steps contained 0.05% Saponin unless otherwise specified. Samples were again washed three times with PBS then incubated in blocking solution (PBS containing 2% BSA) for 1 hr at RT. Afterwards, the cells were incubated in blocking solution containing primary antibodies for 1 hr at RT (EnCOR Chicken-anti-GFAP at 1:2000, Abcam Rabbit-anti-pRab10 at 1:1000, Neuromab Mouse-anti-Arl13B at 1:2000). Cells were then washed three

times with blocking solution, then incubated for 1 hr at RT with blocking solution containing DAPI and donkey-anti alexa fluor secondary antibodies. Coverslips were then rinsed without saponin in PBS two times, in ddH₂O once, and then mounted with mowiol. All image visualizations and analyses were performed using Fiji (RRID:SCR_002285). Maximum intensity projections, background subtraction, and pRab10 integrated intensity measurements were obtained using CellProfiler (RRID:SCR_007358; McQuin et al., 2018).

Statistics: Graphs were made using Graphpad Prism 6 software (GraphPad Prism, RRID:SCR_002798). Error bars indicate SEM. Unless otherwise specified, a Student's T-test was used to test significance. Brains were harvested in Dundee and analyzed at Stanford; identities were blinded for unbiased analyses. RNA hybridization was quantified using CellProfiler (RRID:SCR_007358; McQuin et al., 2018).

568 **KEY RESOURCES. Primary antibodies and reagents used in this study**

569

KEY RESOURCES TABLE				
Reagent type (species) or resource	Designation	Source or reference	Identifiers	Additional information
Genetic reagent (<i>Rattus norvegicus</i>)	SA Sprague Dawley rat	Taconic	#SD-M	NTac:SD Background
Genetic reagent (<i>Rattus norvegicus</i>)	Human LRRK2 G2019S rat	Taconic	#10681	NTac:SD Background; BAC Transgene
Genetic reagent (<i>Mus musculus</i>)	Tg(LRRK2*G2019S)2AMjf	Jackson Laboratory	#018785	C57BL/6 Background; BAC Transgene
Genetic reagent (<i>Mus musculus</i>)	Constitutive KI <i>Lrrk2</i> ^{tm4.1Arte}	Taconic	#13940	C57BL/6 Background; G2019S KI
Genetic reagent (<i>Mus musculus</i>)	B6.Cg- <i>Lrrk2</i> ^{tm1.1Shn} /J	Jackson Laboratory	#009346, RRID:IMSR_JAX:009346	C57BL/6 Background; R1441C KI
Genetic reagent (<i>Mus musculus</i>)	<i>Ppm1h</i> ^{-/-} mouse	Taconic	#TF3142	C57BL/6 Background
Antibody	anti-Arl13B (mouse monoclonal)	Neuromab	N295B/66	(1:1000)
Antibody	anti-Adenylate cyclase III (rabbit polyclonal)	Santa Cruz	SC-588	(1:100)
Antibody	anti-Adenylate cyclase III (rabbit polyclonal)	EnCOR	RPCA-ACIII	(1:10000)

Antibody	anti-NeuN (mouse monoclonal)	Proteintech	66836-1-IG	(1:500)
Antibody	anti-Choline Acetyltransferase (goat polyclonal)	Millipore	AB144P- 1ML	(1:100)
Antibody	anti-GFAP (chicken polyclonal)	Novus Biologicals	NBP1- 05198	(1:2000)
Antibody	anti-GFAP (chicken polyclonal)	EnCOR	CPCA- GFAP	(1:2000)
Antibody	anti-S100B (guinea pig polyclonal)	Synaptic Systems	#287004	(1:200)
Antibody	anti-phospho- Rab10 (Thr73) (rabbit monoclonal)	Abcam	AB230261	(1:1000)
Antibody	anti-Rab10 (mouse monoclonal)	Nanotools	0680– 100/Rab10 -605B11	(1:1000)
Antibody	anti-phospho- Rab12 (Ser105) (rabbit monoclonal)	Abcam	ab256487	(1:1000)
Antibody	anti-Rab12 (sheep polyclonal)	MRC PPU Reagents and Services, University of Dundee	SA227	(1:1000)
Antibody	Anti-phospho- LRRK2 (Ser935) (rabbit monoclonal)	MRC PPU Reagents and Services, University of Dundee	UDD2	(1:1000)
Antibody	Anti-LRRK2 (mouse monoclonal)	Antibodies Inc./NeuroM ab	75-253	(1:1000)

Antibody	anti-PPM1H (sheep polyclonal)	MRC PPU Reagents and Services, University of Dundee	DA018	(1:1000)
Chemical compound, drug	MLi-2	MRC PPU Reagents and Services, University of Dundee		
Commercial assay or kit	RNAscope® Multiplex Fluorescent Reagent Kit v2	Advanced Cell Diagnostics	#323100	
Commercial assay or kit	RNAscope® 3- plex Negative Control Probe	Advanced Cell Diagnostics	#320871	
Commercial assay or kit	RNAscope® Probe - Mm- <i>Gli1</i>	Advanced Cell Diagnostics	#311001	
Commercial assay or kit	RNAscope® Probe - Mm- <i>GDNF</i>	Advanced Cell Diagnostics	#421951	1:10
Commercial assay or kit	OPAL 690 REAGENT PACK	Akoya Biosciences	FP1497001K T	(1:750)
Other		Research Diets, Inc.	D01060501	Untreated diet
Other		Research Diets, Inc.	D01060501 added with 360 mg MLi-2 per kg	Modified diet
Software, Algorithm	FIJI	PMID: 29187165	RRID:SCR_0 02285	
Software, Algorithm	CellProfiler	PMID: 29969450	RRID:SCR_ 007358	

References

- Alessi DR, Sammler E. 2018. LRRK2 kinase in Parkinson's disease. *Science* 360(6384):36-37.
- Arellano JI, Guadiana SM, Breunig JJ, Rakic P, Sarkisian MR. 2012. Development and distribution of neuronal cilia in mouse neocortex. *J Comp Neurol* 520:848–873.
- Bangs F, Anderson KV. 2017. Primary Cilia and Mammalian Hedgehog Signaling. *Cold Spring Harb Perspect Biol.* 9(5):a028175.
- Barroso-Chinea P, Cruz-Muros I, Aymerich MS, Rodríguez-Díaz M, Afonso-Oramas D, Lanciego JL, González-Hernández T. 2005. Striatal expression of GDNF and differential vulnerability of midbrain dopaminergic cells. *Eur J Neurosci.* 21(7):1815-27.
- Berndsen K, Lis P, Yeshaw WM, Wawro PS, Nirujogi RS, Wightman M, Macartney T, Dorward M, Knebel A, Tonelli F, Pfeffer SR, Alessi DR. 2019. PPM1H phosphatase counteracts LRRK2 signaling by selectively dephosphorylating Rab proteins. *Elife* 8:e50416.
- Bowie E, Goetz SC. 2020. TTBK2 and primary cilia are essential for the connectivity and survival of cerebellar Purkinje neurons. *Elife* 2020 9:e51166.
- Chen C, Soto G, Dumrongprechachan V, Bannon N, Kang S, Kozorovitskiy Y, Parisiadou L. 2020. Pathway-specific dysregulation of striatal excitatory synapses by LRRK2 mutations. *Elife* 2020 Oct 2;9:e58997.
- Citri A, Yarden Y. 2006. EGF-ERBB signalling: towards the systems level. *Nat Rev Mol Cell Biol.* 7(7):505-16.
- Corbit KC, Aanstad P, Singla V, Norman AR, Stainier DYR, Reiter JF. 2005. Vertebrate Smoothed functions at the primary cilium. *Nature* 437:1018–1021.
- Dhekne HS, Yanatori I, Gomez RC, Tonelli F, Diez F, Schüle B, Steger M, Alessi DR, Pfeffer SR. 2018. A pathway for Parkinson's disease LRRK2 kinase to block primary cilia and sonic hedgehog signaling in the brain. *Elife* 7:e40202.
- Dhekne HS, Yanatori I, Vides EG, Sobu Y, Diez F, Tonelli F, Pfeffer SR. 2021. LRRK2-phosphorylated Rab10 sequesters Myosin Va with RILPL2 during ciliogenesis blockade. *Life Sci Alliance* 4(5):e202101050. doi: 10.26508/lsa.202101050.
- Djukic B, Casper KB, Philpot BD, Chin L-S, McCarthy KD. 2007. Conditional Knock-Out of Kir4.1 Leads to Glial Membrane Depolarization, Inhibition of Potassium and Glutamate Uptake, and Enhanced Short-Term Synaptic Potentiation. *J Neurosci* 27:11354–11365.
- Domingo A, Klein C. 2018. Genetics of Parkinson disease, *Handbook of Clinical Neurology*.
- Dvorzhak A, Vagner T, Kirmse K, Grantyn R. 2016. Functional Indicators of Glutamate Transport in Single Striatal Astrocytes and the Influence of Kir4.1 in Normal and Huntington Mice. *J Neurosci* 36:4959–4975.
- Farmer WT, Abrahamsson T, Chierzi S, Lui C, Zaelzer C, Jones EV, Bally BP, Chen GG, Théroux JF, Peng J, Bourque CW, Charron F, Ernst C, Sjöström PJ, Murai KK. 2016.

606 Neurons diversify astrocytes in the adult brain through sonic hedgehog signaling. *Science*
607 351(6275):849-54.

608 Fell MJ, Mirescu C, Basu K, Cheewatrakoolpong B, DeMong DE, Ellis JM, Hyde LA, Lin Y,
609 Markgraf CG, Mei H, Miller M, Poulet FM, Scott JD, Smith MD, Yin Z, Zhou X, Parker EM,
610 Kennedy ME, Morrow JA. 2015. MLI-2, a Potent, Selective, and Centrally Active
611 Compound for Exploring the Therapeutic Potential and Safety of LRRK2 Kinase Inhibition.
612 *J Pharmacol Exp Ther.* 355(3):397-409.

613 Foo LC, Allen NJ, Bushong EA, Ventura PB, Chung WS, Zhou L, Cahoy JD, Daneman R, Zong
614 H, Ellisman MH, Barres BA. 2011. Development of a method for the purification and
615 culture of rodent astrocytes. *Neuron* 71(5):799-811.

616 Gilliam D, O'Brien DP, Coates JR, Johnson GS, Johnson GC, Mhlanga-Mutangadura T, Hansen
617 L, Taylor JF, Schnabel RD. 2014. A homozygous KCNJ10 mutation in Jack Russell
618 Terriers and related breeds with spinocerebellar ataxia with myokymia, seizures, or both. *J*
619 *Vet Intern Med* 3:871-7.

620 Gomez RC, Wawro P, Lis P, Alessi DR, Pfeffer SR. 2019. Membrane association but not
621 identity is required for LRRK2 activation and phosphorylation of Rab GTPases. *J Cell Biol*
622 218:4157–4170.

623 Gonzalez-Reyes LE, Verbitsky M, Blesa J, Jackson-Lewis V, Paredes D, Tillack K, Phani S,
624 Kramer ER, Przedborski S, Kottmann AH. 2012. Sonic Hedgehog Maintains Cellular and
625 Neurochemical Homeostasis in the Adult Nigrostriatal Circuit. *Neuron* 75:306–319.

626 Greggio E, Jain S, Kingsbury A, Bandopadhyay R, Lewis P, Kaganovich A, van der Brug MP,
627 Beilina A, Blackinton J, Thomas KJ, Ahmad R, Miller DW, Kesavapany S, Singleton A,
628 Lees A, Harvey RJ, Harvey K, Cookson MR. 2006. Kinase activity is required for the toxic
629 effects of mutant LRRK2/dardarin. *Neurobiol Dis* 23:329–341.

630 Guo J, Otis JM, Higginbotham H, Monckton C, Cheng J, Asokan A, Mykytyn K, Caspary T,
631 Stuber GD, Anton ES. 2017. Primary Cilia Signaling Shapes the Development of
632 Interneuronal Connectivity. *Dev Cell* 42:286-300.e4.

633 Hidalgo-Figueroa M, Bonilla S, Gutierrez F, Pascual A, and Lopez- Barneo, J. 2012. GDNF is
634 predominantly expressed in the PV+ neostriatal interneuronal ensemble in normal mouse
635 and after injury of the nigrostriatal pathway. *J. Neurosci.* 32, 864–872.

636 Hill SA, Blaeser AS, Coley AA, Xie Y, Shepard KA, Harwell CC, Gao W-J, Garcia ADR. 2019.
637 Sonic hedgehog signaling in astrocytes mediates cell type-specific synaptic organization.
638 *Elife* 8:e45545.

639 Iannotta L, Biosa A, Kluss JH, et al. 2020. Divergent Effects of G2019S and R1441C LRRK2
640 Mutations on LRRK2 and Rab10 Phosphorylations in Mouse Tissues. *Cells* 9(11):2344.

641 Inyushin M, Kucheryavykh LY, Kucheryavykh YV, Nichols CG, Buono RJ, Ferraro TN,
642 Skatchkov SN, Eaton MJ. 2010. Potassium channel activity and glutamate uptake are
643 impaired in astrocytes of seizure-susceptible DBA/2 mice. *Epilepsia* 9:1707-13.

644 Ishii S, Sasaki T, Mohammad S, Hwang H, Tomy E, Somaa F, Ishibashi N, Okano H, Rakic P,
645 Hashimoto-Torii K, Torii M. (2021). Primary cilia safeguard cortical neurons in neonatal
646 mouse forebrain from environmental stress-induced dendritic degeneration. *Proc Natl*
647 *Acad Sci U S A* 118:1.

648 Ito G, Katsemonova K, Tonelli F, Lis P, Baptista MAS, Shpiro N, Duddy G, Wilson S, Ho PW-L,
649 Ho S-L, Reith AD, Alessi DR. 2016. Phos-tag analysis of Rab10 phosphorylation by
650 LRRK2: a powerful assay for assessing kinase function and inhibitors. *Biochem J*
651 473:2671–2685.

652 Jaleel M, Nichols RJ, Deak M, Campbell DG, Gillardon F, Knebel A, Alessi DR. 2007. LRRK2
653 phosphorylates moesin at threonine-558: characterization of how Parkinson's disease
654 mutants affect kinase activity. *Biochem J*. 405:307-17.

655 Kalogeropoulou AF, Freemantle JB, Lis P, Vides EG, Polinski NK, Alessi DR. 2020. Endogenous
656 Rab29 does not impact basal or stimulated LRRK2 pathway activity. *Biochem J*.
657 477(22):4397-4423.

658 Kasahara K, Miyoshi K, Murakami S, Miyazaki I, Asanuma M. 2014. Visualization of astrocytic
659 primary cilia in the mouse brain by immunofluorescent analysis using the cilia marker
660 Arl13B. *Acta Med Okayama* 68:317–22.

661 Kelly K, Wang S, Boddu R, Liu Z, Moukha-Chafiq O, Augelli-Szafran C, West AB. 2018. The
662 G2019S mutation in LRRK2 imparts resiliency to kinase inhibition. *Exp Neurol*. 309:1-13.

663 Khakh BS, Deneen B. 2019. The Emerging Nature of Astrocyte Diversity. *Annu Rev Neurosci*
664 42:187–207.

665 Khan SS, Dhekne HS, Tonelli F, Pfeffer, SP. 2020. Analysis of Primary Cilia in Rodent Brain By
666 Immunofluorescence Microscopy. *protocols.io*
667 <https://dx.doi.org/10.17504/protocols.io.bnwmfce>

668 Kluss, J.H., Mazza, M.C., Li, Y. *et al.* 2021. Preclinical modeling of chronic inhibition of the
669 Parkinson's disease associated kinase LRRK2 reveals altered function of the
670 endolysosomal system in vivo. *Mol Neurodegeneration* **16**, 17.

671 Kong JH, Siebold C, Rohatgi R. 2019. Biochemical mechanisms of vertebrate hedgehog
672 signaling. *Development*. 146(10):dev166892.

673 Kuwahara T, Inoue K, D'Agati VD, Fujimoto T, Eguchi T, Saha S, Wolozin B, Iwatsubo T,
674 Abeliovich A. 2016. LRRK2 and RAB7L1 coordinately regulate axonal morphology and
675 lysosome integrity in diverse cellular contexts. *SciRep* 6:29945

676 Lee H, James WS, Cowley SA. 2017. LRRK2 in peripheral and central nervous system innate
677 immunity: its link to Parkinson's disease. *Biochem Soc Trans* 45:131–139.

678 Lex RK, Ji Z, Falkenstein KN, Zhou W, Henry JL, Ji H, Vokes SA. 2020. GLI transcriptional
679 repression regulates tissue-specific enhancer activity in response to Hedgehog signaling.
680 *Elife*. 2020;9:e50670.

681 Li X, Patel JC, Wang J, Avshalumov M V., Nicholson C, Buxbaum JD, Elder GA, Rice ME, Yue
682 Z. 2010. Enhanced striatal dopamine transmission and motor performance with LRRK2
683 overexpression in mice is eliminated by familial Parkinson's disease mutation G2019S. *J*
684 *Neurosci* 30:1788–1797.

685 Linhart R, Wong S, Cao J, Tran M, Huynh A, Ardrey C, Park J, Hsu C, Taha S, Peterson R,
686 Shea S, Kurian J, Venderova K. 2014. Vacuolar protein sorting 35 (Vps35) rescues
687 locomotor deficits and shortened lifespan in *Drosophila* expressing a Parkinson's disease
688 mutant of Leucine-rich repeat kinase 2 (LRRK2). *Mol Neurodegener* 9:23.

689 Lis P, Burel S, Steger M, Mann M, Brown F, Diez F, Tonelli F, Holton JL, Ho PW, Ho SL, Chou
690 MY, Polinski NK, Martinez TN, Davies P, Alessi DR. 2018. Development of phospho-
691 specific Rab protein antibodies to monitor *in vivo* activity of the LRRK2 Parkinson's
692 disease kinase. *Biochem J.* 475(1):1-22.

693 Liu Z, Bryant N, Kumaran R, Beilina A, Abeliovich A, Cookson MR, West AB. 2018. LRRK2
694 phosphorylates membrane-bound Rabs and is activated by GTP-bound Rab7L1 to
695 promote recruitment to the trans-Golgi network. *Hum Mol Genet* 27:385–395.

696 Madero-Pérez J, Fdez E, Fernández B, Lara Ordóñez AJ, Blanca Ramírez M, Gómez-Suaga P,
697 Waschbüsch D, Lobbestael E, Baekelandt V, Nairn AC, Ruiz-Martínez J, Aiausti A, López
698 de Munain A, Lis P, Comptdaer T, Taymans J-M, Chartier-Harlin M-C, Beilina A, Gonnelli
699 A, Cookson MR, Greggio E, Hilfiker S. 2018. Parkinson disease-associated mutations in
700 LRRK2 cause centrosomal defects via Rab8a phosphorylation. *Mol Neurodegener* 13:3.

701 Malave L, Zuelke DR, Uribe-Cano S, Starikov L, Rebholz H, Friedman E, Qin C, Li Q, Bezard E,
702 Kottmann AH. 2021. Dopaminergic co-transmission with sonic hedgehog inhibits
703 abnormal involuntary movements in models of Parkinson's disease and L-Dopa induced
704 dyskinesia. *Commun Biol.* 4(1):1071.

705 Mandemakers W, Snellinx A, O'Neill MJ, de Strooper B. 2012. LRRK2 expression is enriched in
706 the striosomal compartment of mouse striatum. *Neurobiol Dis* 48:582–593.

707 Martín R, Bajo-Grañeras R, Moratalla R, Perea G, Araque A. 2015. Circuit-specific signaling in
708 astrocyte-neuron networks in basal ganglia pathways. *Science* 349:730–734.

709 McQuin C, Goodman A, Chernyshev V, Kametsky L, Cimini BA, Karhohs KW, Doan M, Ding L,
710 Rafelski SM, Thirstrup D, Wiegraebe W, Singh S, Becker T, Caicedo JC, Carpenter AE.
711 2018. CellProfiler 3.0: Next-generation image processing for biology. *PLoS Biol.*
712 16(7):e2005970.

713 Mir R, Tonelli F, Lis P, Macartney T, Polinski NK, Martinez TN, Chou MY, Howden AJM, König
714 T, Hotzy C, Milenkovic I, Brücke T, Zimprich A, Sammler E, Alessi DR. 2018. The
715 Parkinson's disease VPS35[D620N] mutation enhances LRRK2-mediated Rab protein
716 phosphorylation in mouse and human. *Biochem J* 475:1861–1883.

717 Nirujogi RS, Tonelli F, Taylor M, Lis P, Zimprich A, Sammler E, Alessi DR. 2021. Development
718 of a multiplexed targeted mass spectrometry assay for LRRK2-phosphorylated Rabs and
719 Ser910/Ser935 biomarker sites. *Biochem J.* 478(2):299-326.

720 Ordóñez LAJ, Fernández B, Fdez E, Romo-Lozano M, Madero-Pérez J, Lobbestael E,
 721 Baekelandt V, Aiastui A, López de Munaín A, Melrose HL, Civiero L, Hilfiker S. 2019.
 722 RAB8, RAB10 and RILPL1 contribute to both LRRK2 kinase-mediated centrosomal
 723 cohesion and ciliogenesis deficits. *Hum Mol Genet* 28:3552–3568.

724 Pfeffer SR. 2018. LRRK2 and Rab GTPases. *Biochem Soc Trans* 46:1707–1712.

725 Pfeffer SR. 2017. Rab GTPases: master regulators that establish the secretory and endocytic
 726 pathways. *Mol Biol Cell* 28:712–715.

727 Poewe W, Seppi K, Tanner CM, Halliday GM, Brundin P, Volkman J, Schrag A-E, Lang AE.
 728 2017. Parkinson disease. *Nat Rev Dis Prim* 3:17013.

729 Purlyte E, Dhekne HS, Sarhan AR, Gomez R, Lis P, Wightman M, Martinez TN, Tonelli F,
 730 Pfeffer SR, Alessi DR. 2018. Rab29 activation of the Parkinson's disease- associated
 731 LRRK2 kinase. *EMBO J* 37:1–18.

732 Rohatgi R, Milenkovic L, Scott MP. 2007. Patched1 Regulates Hedgehog Signaling at the
 733 Primary Cilium. *Science* 317:372–376.

734 Rueden CT, Schindelin J, Hiner MC, DeZonia BE, Walter AE, Arena ET, Eliceiri KW. 2017.
 735 ImageJ2: ImageJ for the next generation of scientific image data. *BMC Bioinformatics*.
 736 18(1):529.

737 Scholl UI, Choi M, Liu T, Ramaekers VT, Häusler MG, Grimmer J, Tobe SW, Farhi A, Nelson-
 738 Williams C, Lifton RP. 2009. Seizures, sensorineural deafness, ataxia, mental retardation,
 739 and electrolyte imbalance (SeSAME syndrome) caused by mutations in KCNJ10. *Proc*
 740 *Natl Acad Sci U S A* 106:5842–584.

741 Sibille J, Pannasch U, Rouach N. 2014. Astroglial potassium clearance contributes to short-term
 742 plasticity of synaptically evoked currents at the tripartite synapse. *J Physiol* 592:87–102.

743 Sipos É, Komoly S, Ács P. 2018. Quantitative Comparison of Primary Cilia Marker Expression
 744 and Length in the Mouse Brain. *J Mol Neurosci* 64:397–409.

745 Sobu Y, Wawro PS, Dhekne HS, Pfeffer, SR. 2021. Pathogenic LRRK2 regulates ciliation
 746 probability upstream of Tau Tubulin kinase 2. *Proc Natl Acad Sci. USA*, in press. bioRxiv
 747 2020.04.07.029983

748 Steger M, Diez F, Dhekne HS, Lis P, Nirujogi RS, Karayel O, Tonelli F, Martinez TN, Lorentzen
 749 E, Pfeffer SR, Alessi DR, Mann M. 2017. Systematic proteomic analysis of LRRK2-
 750 mediated rab GTPase phosphorylation establishes a connection to ciliogenesis. *Elife*
 751 6:e31012.

752 Steger M, Tonelli F, Ito G, Davies P, Trost M, Vetter M, Wachter S, Lorentzen E, Duddy G,
 753 Wilson S, Baptista MAS, Fiske BK, Fell MJ, Morrow JA, Reith AD, Alessi DR, Mann M.
 754 2016. Phosphoproteomics reveals that Parkinson's disease kinase LRRK2 regulates a
 755 subset of Rab GTPases. *Elife* 5:e12813.

756 Sterpka A, Chen X. 2018. Neuronal and astrocytic primary cilia in the mature brain. *Pharmacol*
 757 *Res* 137:114–121.

758 Tong X, Ao Y, Faas GC, Nwaobi SE, Xu J, Haustein MD, Anderson MA, Mody I, Olsen ML,
759 Sofroniew M V, Khakh BS. 2014. Astrocyte Kir4.1 ion channel deficits contribute to
760 neuronal dysfunction in Huntington's disease model mice. *Nat Neurosci* 17:694–703.

761 Waschbüsch D, Purlyte E, Pal P, McGrath E, Alessi DR, Khan AR. 2020. Structural Basis for
762 Rab8a Recruitment of RILPL2 via LRRK2 Phosphorylation of Switch 2. *Structure* 28:406-
763 417.e6.

764 West AB, Moore DJ, Biskup S, Bugayenko A, Smith WW, Ross CA, Dawson VL, Dawson TM.
765 2005. Parkinson's disease-associated mutations in leucine-rich repeat kinase 2 augment
766 kinase activity. *Proc Natl Acad Sci USA* 102:16842–16847.

767 West AB, Cowell RM, Daher JP, Moehle MS, Hinkle KM, Melrose HL, Standaert DG, Volpicelli-
768 Daley LA. 2014. Differential LRRK2 expression in the cortex, striatum, and substantia
769 nigra in transgenic and nontransgenic rodents. *J Comp Neurol.* 522(11):2465-80.

770 Zhai S, Tanimura A, Graves SM, Shen W, Surmeier DJ. 2018. Striatal synapses, circuits, and
771 Parkinson's disease. *Curr Opin Neurobiol* 48:9–16.

772 Zhang Y, Chen K, Sloan SA, Bennett ML, Scholze AR, O'Keefe S, Phatnani HP, Guarnieri P,
773 Caneda C, Ruderisch N, Deng S, Liddel SA, Zhang C, Daneman R, Maniatis T, Barres
774 BA, Wu JQ. 2014. An RNA-Sequencing Transcriptome and Splicing Database of Glia,
775 Neurons, and Vascular Cells of the Cerebral Cortex. *J Neurosci* 34:11929–11947.

776

Figure Legends

Fig. 1. G2019S LRRK2 Striatal Cholinergic Interneurons have fewer primary cilia. A.

Confocal images of sections of the dorsal striatum from 13-month G2019S LRRK2 KI mice; Cholinergic Acetyltransferase (ChAT) (green, white outline); Adenylate cyclase 3 (AC3) (magenta, white box), and DAPI (blue). **B.** Percentage of ChAT⁺ neurons containing a cilium. Wild type, light gray; G2019S KI, dark gray as indicated. **C.** Quantitation of ChAT⁺ neuron ciliary length from sections as in A. **D.** Confocal images of sections of the dorsal striatum of 10-month G2019S LRRK2 BAC Tg mice; ChAT (green, white outline), AC3 (magenta, white box), and neuron specific nuclear antigen, NeuN (blue). **E.** Percentage of G2019S LRRK2 BAC or wild type ChAT⁺ interneurons containing a cilium. **F.** Quantitation of ChAT⁺ neuron ciliary length. Scale bar, 10 μ m. Significance was determined by t-test; (B) **, P = 0.0016; (E) ***, P = 0.0001. Values represent the data from individual brains, analyzing 4-5 brains per group, 2-3 sections per mouse, and >30 neurons per mouse.

Figure 1-Figure Supplement 1. Cilia Density and Cilia Length in G2019S LRRK2 and Wild

Type Mice. A. Quantitation of cilia density for all cells marked by DAPI staining in the cortex, hippocampus and striatum of 13-month G2019S LRRK2 KI (GS KI) or wild type (WT) mice. **B.** Quantitation of cilia length for DAPI stained cells in the cortex, hippocampus and striatum of 13-month GS KI or WT mice. **C.** Quantitation of NeuN⁺ neurons with cilia in the dorsal striatum of 13-month GS KI and WT mice (left bars) or 10-month GS BAC and WT mice (right bars). Significance was determined by t-test for 2-3 tissue sections per genotype; >50 cells per brain region.

Fig. 2 G2019S LRRK2 Striatal Astrocytes have fewer primary cilia. A. Confocal images of sections of the dorsal striatum from 13-month G2019S LRRK2 KI mice; astrocyte marker, Glial fibrillary acidic protein (GFAP) (magenta, white outline), cilia marker, ADP-ribosylation factor-like

protein 13B (Arl13B) (green, white box), and DAPI (blue). **B., C.**, Quantitation of the percentage of astrocytes containing a cilium and astrocyte ciliary length from sections described in A. **D.** Confocal images of sections of the dorsal striatum from 10-month G2019S LRRK2 BAC Tg mice, antibody labeled for Glial fibrillary acidic protein (GFAP, magenta, white box), Arl13B (green, white box), and stained with DAPI (blue). **E, F.** Quantitation of the percentage of astrocytes containing a cilium and astrocyte ciliary length from sections described in D. Scale bars, 10 μ m. Values represent 4-5 brains per group, 2-3 sections per mouse, and >30 astrocytes per mouse. Significance was determined by t-test; B, **, P = 0.0011; E, ** P = 0.0054; F, **** P < 0.0001.

Fig. 3. Two weeks MLI-2 treatment does not alter ciliogenesis in R1441C LRRK2 striatal interneurons or astrocytes. Mice (8-weeks old) were fed MLI-2 LRRK2 inhibitor-containing chow or control chow for two consecutive weeks prior to perfusion and staining. **A.** Confocal images of sections of the dorsal striatum from 8 week R1441C LRRK2 KI mice; ChAT (green, white outline); Adenylate cyclase 3 (AC3) (magenta), and DAPI (blue). **B.** Quantitation of the percentage of ChAT⁺ and ChAT⁻ neurons containing a cilium. **C.** Percentage of ChAT⁺ neurons containing a cilium \pm MLI-2. **D.** Quantitation of ChAT⁺ neuron ciliary length. **E.** Confocal images of Astrocytes identified by antibodies to GFAP (magenta, white outline), Arl13B (green), and DAPI (blue), \pm MLI-2. **F., G.** Quantitation of the percentage of total astrocytes (F) or GFAP/S100B⁺ astrocytes (G) containing a cilium. Scale bars, 10 μ m. Significance was determined by t-test. B, *, P = 0.0417.

Fig. 4. Two weeks of MLI-2 treatment decreases LRRK2 pS935 but does not alter Rab10 phosphorylation in R1441C LRRK2 mouse brain. **A and B.** Littermate- or age-matched LRRK2 R1441C homozygous knock-in mice were fed either a control diet or MLI-2-containing diet for 14 days prior to tissue collection. Two mice from each group were perfused with PBS

only; brains collected from these mice were snap frozen in liquid nitrogen and used to monitor inhibition of LRRK2 activity by immunoblotting. **A.** 40 µg brain tissue extract was subjected to immunoblot analysis with antibodies specific for the indicated antigens. Duplicate samples were analyzed using the LI-COR Odyssey CLx imaging system. **B.** Quantitation of data in A, calculated using Image Studio software (mean ± SD, normalized to control diet fed animals.) **C.** 11 C57BL/6j wild-type mice received either control diet or diet containing MLI-2, targeted to provide a concentration of 60 mg/kg per day for 14 days. On the last day, 3 mice from the control diet group received 30mg/kg MLI-2 dissolved in 40% (w/v) (2-hydroxypropyl)- β-cyclodextrin via subcutaneous injection for 2 hrs prior to tissue collection. 40 µg brain tissue extract was subjected to quantitative immunoblotting analysis with the indicated antibodies. Each lane represents a tissue sample from a different animal.

Fig. 5. PPM1H mutant Striatal cholinergic neurons and astrocytes have fewer primary cilia. **A.** Confocal images of sections from 5.5-month *Ppm1h*^{+/+} or 2.5-month *Ppm1h*^{-/-} mice compared with corresponding age-matched WT mice; ChAT (green, white outline); AC3 (magenta, yellow arrowhead), and DAPI (blue). **B.** Percentage of ChAT⁺ neurons of the indicated genotype containing a cilium. Wild type, light gray; *Ppm1h* mutant, dark gray as indicated. **C.** Confocal images of sections of the dorsal striatum from mice described in A and B as indicated; GFAP (magenta, white outline), Arl13B (green, yellow arrowhead), and DAPI (blue). **D.** Percentage of GFAP⁺ astrocytes containing a cilium. Wild type, light gray; *Ppm1h*^{+/+} or *Ppm1h*^{-/-}, dark gray as indicated. Scale bars, 10 µm. Significance was determined by t-test; (B) WT vs *Ppm1h*^{+/+}; **, P =0.0018. (C) WT vs *Ppm1h*^{-/-}; ***, P =0.0007. (D) WT vs *Ppm1h*^{+/+}; **, P =0.0032. WT vs *Ppm1h*^{-/-}; ***, P =0.0002. *Ppm1h*^{+/+} vs *Ppm1h*^{-/-}; ns, P =0.3474. Values represent the data from individual brains, analyzing 4 brains per group, 2-3 sections per mouse, and >30 cells per mouse. Significance was determined either by student's t-test or by Ordinary one-way ANOVA using Dunnett's multiple comparisons test. Scale bars, 10µm.

Figure 5- Figure Supplement 1. Wildtype and PPM1H heterozygous or homozygous knock-out mice were treated with vehicle (40% (w/v) (2-hydroxypropyl)- β -cyclodextrin) or 30 mg/kg MLI-2 dissolved in vehicle by subcutaneous injection 2 hr prior to tissue collection. 40 μ g brain tissue extract was analyzed by quantitative immunoblotting analysis with the indicated antibodies. Each lane represents extract from a different mouse.

Fig. 6. *Gli1* expression in R1441C LRRK2 Dorsal Striatal Cholinergic Interneurons is cilia dependent and enhanced

A. 10-month WT mouse dorsal striatum was subjected to *in situ* hybridization using a *Gli1* probe (gray dots, highlighted by yellow arrowheads) or a negative control probe. ChAT (green, white outline) and DAPI⁺ nuclei (blue) were detected by immuno- or chemical staining. **B.** 10-month WT or R1441C mouse dorsal striatum was labeled as indicated: ChAT (green, white outline), AC3 (magenta, white arrow), *Gli1* mRNA (gray dots, yellow arrowheads), DAPI (blue). **C.** Average numbers of *Gli1* dots per cell for all cell types in the dorsal striatum. Cell numbers were determined by DAPI staining. Values represent the mean \pm SEM from 4 WT and 4 R1441C brains each containing >500 DAPI stained nuclei from 30 regions. $P = 0.88$. **D.** Average numbers of *Gli1* dots for cholinergic interneurons with or without primary cilia as indicated. Values represent the mean \pm SEM from 4 WT and 5 R1441C brains, each containing 9-32 cells. **E.** Histogram of the number of *Gli1* dots in ciliated cholinergic interneurons from WT or R1441C mice. $P = 0.14$ (0), 0.054 (1-2), *, 0.015 (3-4), 0.79 (5-). Significance was determined by t-test. Arrows indicate primary cilia for ChAT interneurons. Arrowheads indicate *Gli1* mRNA dots. Scale bars, 10 μ m.

Fig 7. *Gli1* expression in astrocytes is cilia dependent

A,B. 10-month R1441C LRRK2 KI mouse dorsal striatum was subjected to *in situ* hybridization using a *Gli1* probe (gray dots, highlighted with yellow arrowheads). Astrocytes were detected with (A) anti-GFAP or (B) anti-S100B (green, white outline); primary cilia were detected with anti-Arl13B (magenta, white arrows). **C,D.** Average numbers of *Gli1* dots from (C) GFAP and (D) S100B⁺ astrocytes with or without primary cilia. **E.** Relative contribution to total *Gli1* dots over GFAP⁺ astrocytes as a function of their ciliation status. Values represent the mean \pm SEM from (C) 4 WT and 3 R1441C brains each containing >35 cells or (D) 3 WT and 3 R1441C brains each containing >21 cells. (C) Ciliated WT vs Unciliated WT: *, $P = 0.020$, Ciliated R1441C vs Ciliated R1441C: **, $P = 0.0032$. (D) Ciliated WT vs Unciliated WT: $P = 0.12$, Ciliated R1441C vs Unciliated R1441C: *, $P = 0.017$. (E) Ciliated WT vs Unciliated WT: ****, $P < 0.0001$; Ciliated R1441C vs Unciliated R1441C: ****, $P < 0.0001$; Unciliated WT vs Unciliated R1441C: ns, $P > 0.9999$. Significance was determined by unpaired t-test. Arrows indicate primary cilia from GFAP or S100B⁺ astrocytes. Scale bars, 10 μ m.

Fig. 8. *Gdnf* expression is cilia dependent and dysregulated in LRRK2 G2019S striatum.

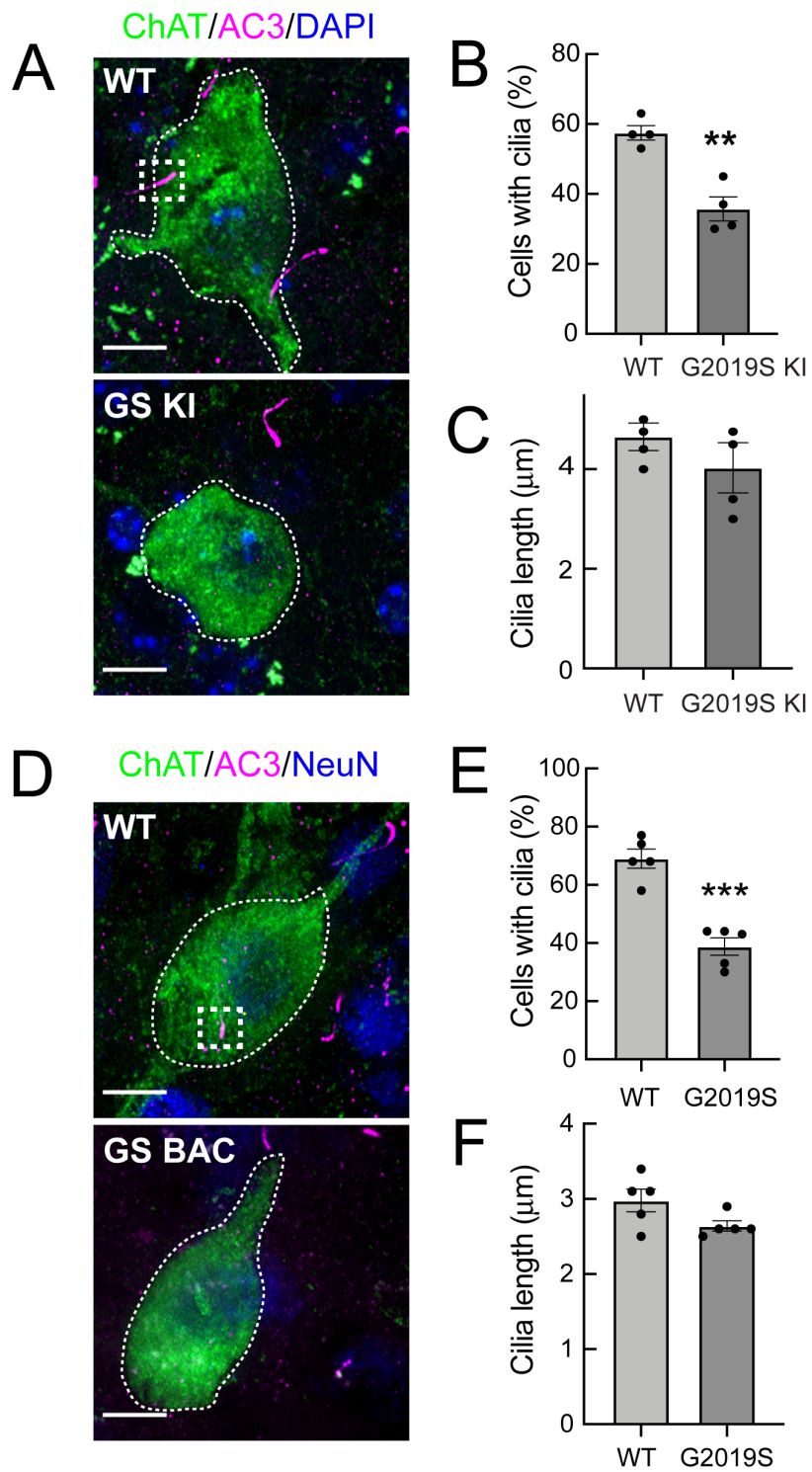
A. 5.5-month WT or LRRK2 G2019S mouse dorsal striatum was subjected to *in situ* hybridization using a *Gdnf* probe (white dots) and immunostained as indicated: ChAT (green, white outline), AC3 (red, yellow arrowheads), DAPI (blue). **B.** Percent of cells with cilia. **C.** Relative level of total *Gdnf* RNA in ChAT⁺ neurons as in A. **D.** Relative contribution to total *Gdnf* dots over cholinergic interneurons as a function of their ciliation status. **E.** Relative contribution to total *Gli1* dots over cholinergic interneurons as a function of their ciliation status in 10-month old WT or R1441C mouse dorsal striatum (as in Fig. 7). Values represent the mean \pm SEM from 4 WT and 4 G2019S brains each containing ≥ 33 cells. (B) WT vs G2019S, ***, $P = 0.0009$. (D) Ciliated WT vs Unciliated WT, ****, $P < 0.0001$. Ciliated WT vs Ciliated G2019S, **, $P = 0.0009$.

904 P =0.0020. Ciliated WT vs Unciliated G2019S; **, P =0.0040. Unciliated WT vs Ciliated
905 G2019S; **, P =0.0040. Unciliated WT vs Unciliated G2019S; **, P =0.0020. (E) Ciliated WT vs.
906 Unciliated WT, ****, P <0.0001. Unciliated WT vs Ciliated R1441C, **, P = 0.0029. Unciliated
907 WT vs Unciliated R1441C, **, P =0.0080; Ciliated WT vs Ciliated R1441C, **, P =0.0080.
908 Significance was determined either by student's t-test or by Ordinary one-way ANOVA using
909 Dunnett's multiple comparisons test. Scale bars, 10µm.

910

911 **Fig 9. Immuno-panned primary G2019S LRRK2 Astrocytes Display Increased pRab10.**

912 BAC Transgenic G2019S^{+/-} LRRK2 rat astrocytes were dissected from P5 pups and cultured for
913 1 week ± 200 nM MLi-2. **A.** Astrocytes were labeled with anti-GFAP and DAPI (blue, white
914 outline); rabbit-anti-phospho-Rab10 (magenta), and anti-Arl13B (green). The boxed regions in
915 the bottom row were enlarged and are shown at the lower right. Top row shows additional
916 examples. **B.** Quantitation of pRab10 intensity in ciliated or unciliated G2019S^{+/-} astrocytes as
917 in B. Unciliated G2019S^{+/-} vs Ciliated G2019S^{+/-}; ***, P=0.0009, Unciliated G2019S^{+/-} vs MLi-2
918 treated Unciliated G2019S^{+/-}; ****, P<0.0001; Unciliated G2019S^{+/-} vs Ciliated MLi-2 treated;
919 ****, P<0.0001; ns = not statistically significant. Significance was determined either by student's
920 t-test or by Ordinary one-way ANOVA using Dunnett's multiple comparisons test. Scale bars,
921 10µm.



Khan et al., Fig. 1

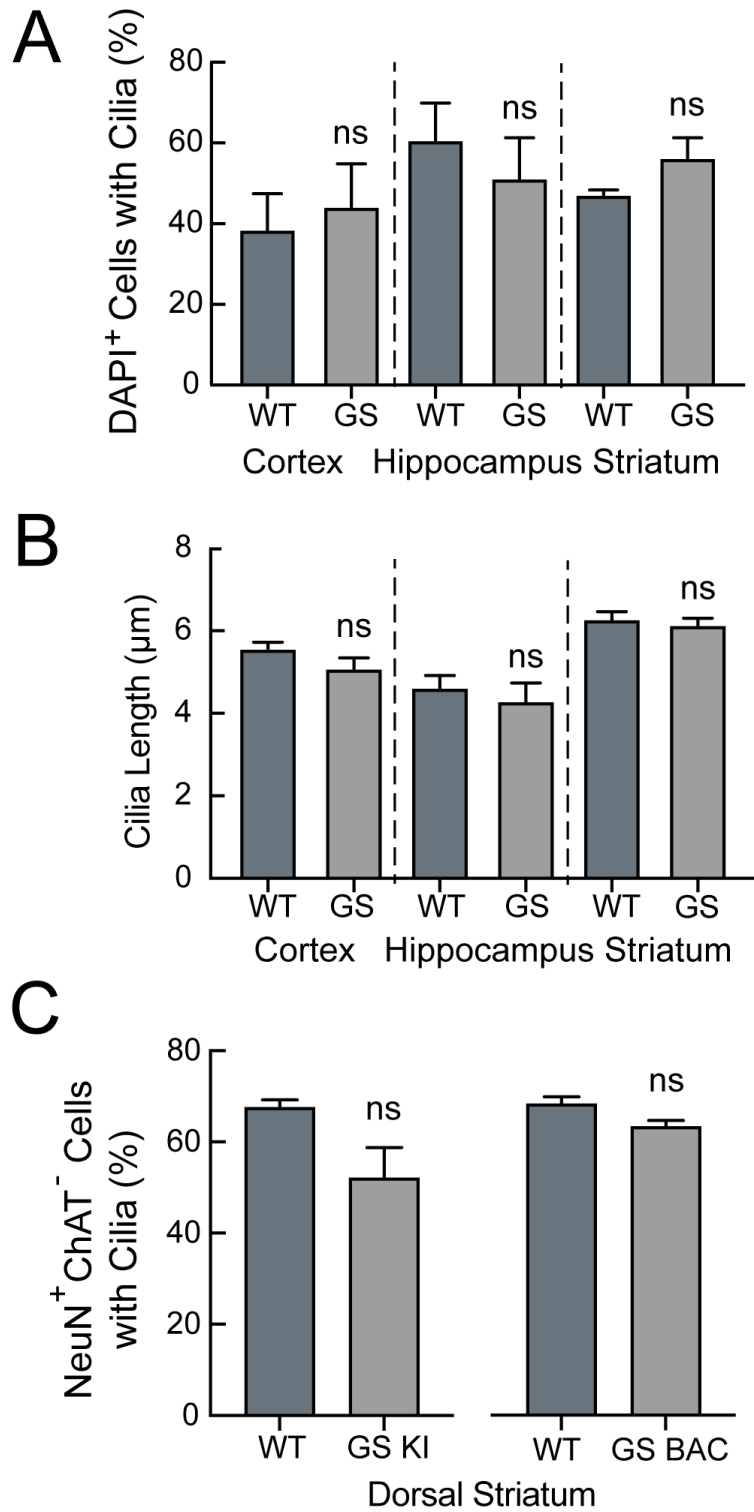
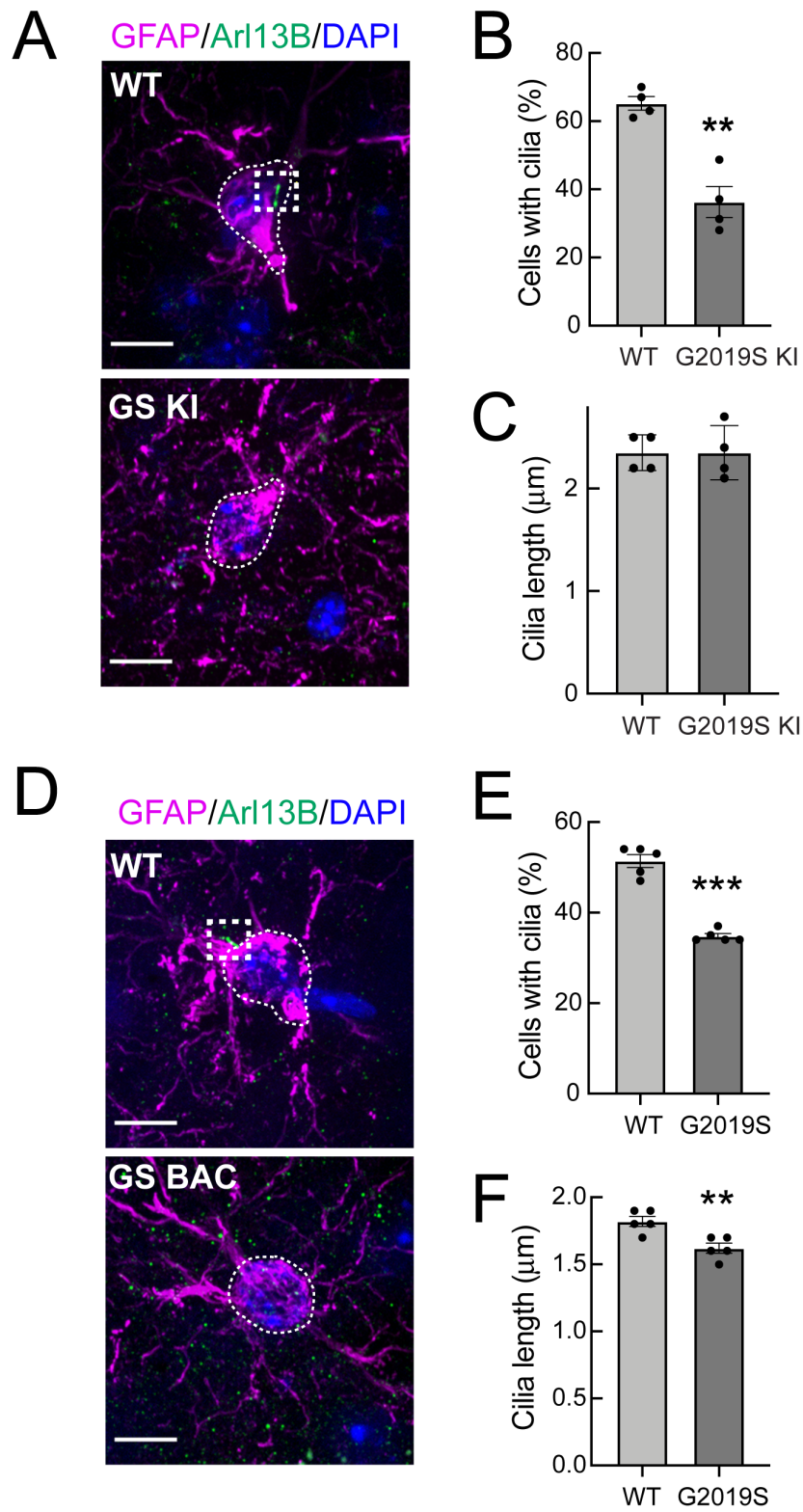
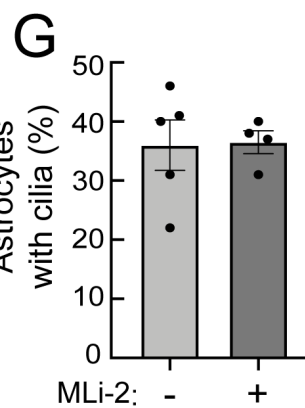
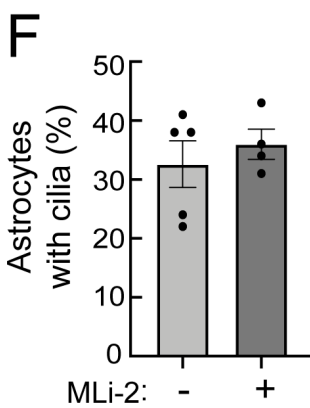
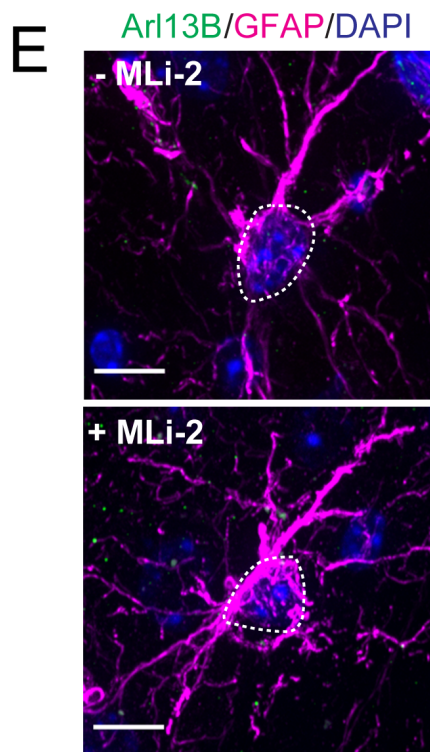
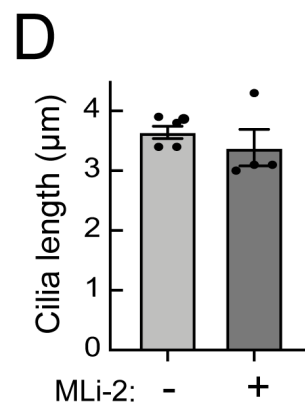
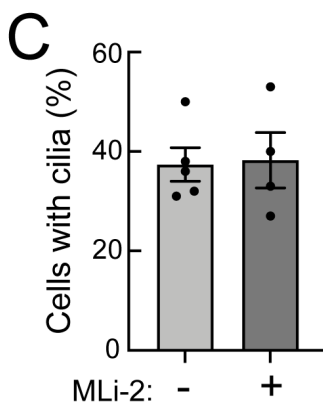
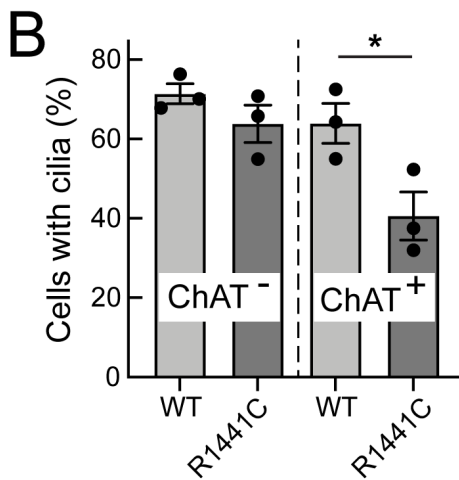
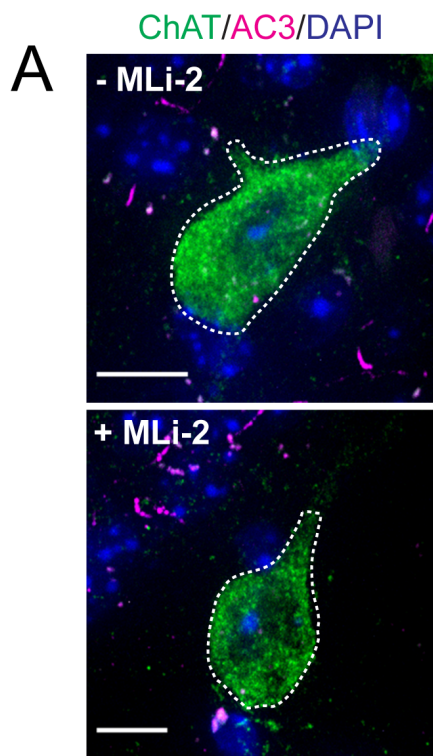
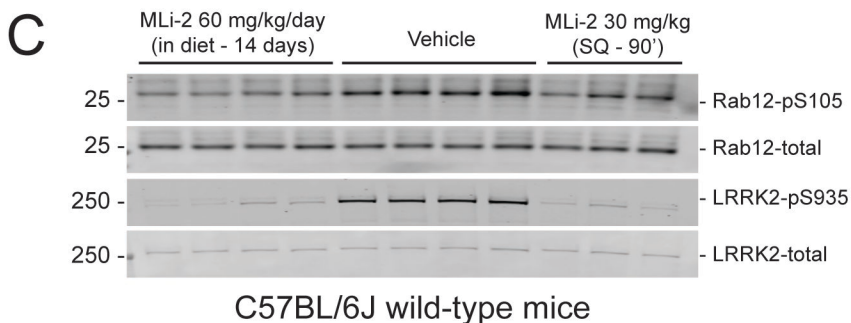
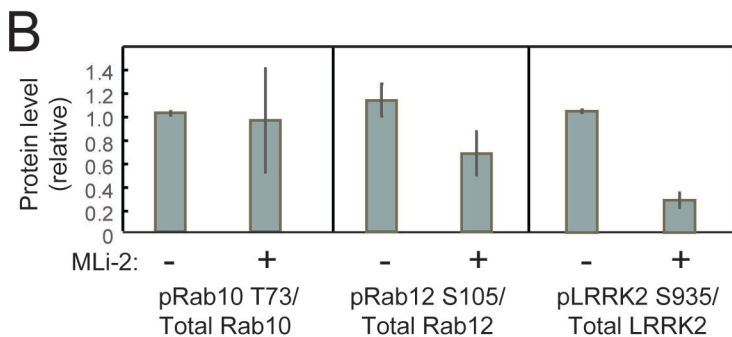
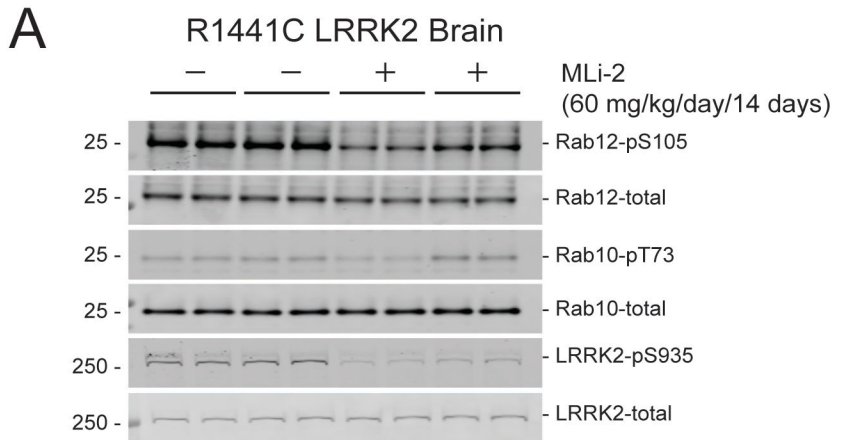


Figure 1-Figure Supplement 1

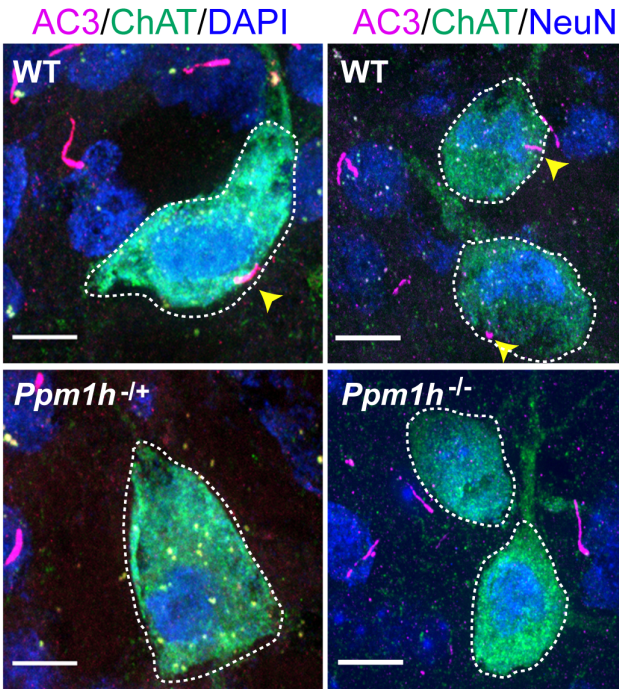


Khan et al., Fig. 2

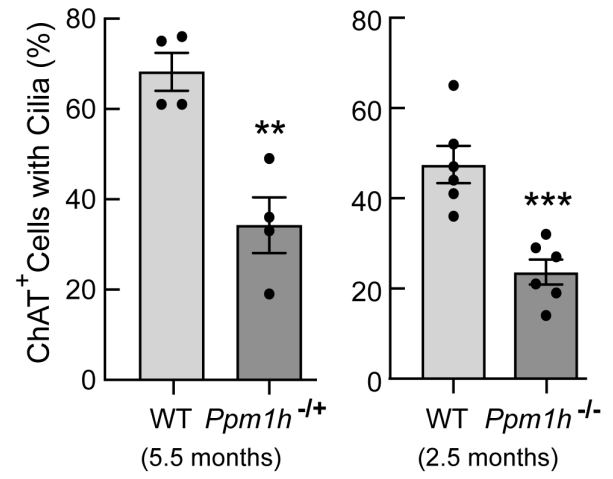




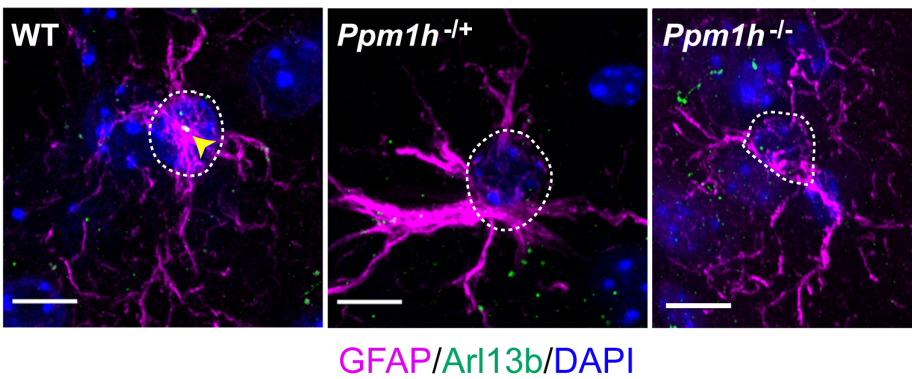
A



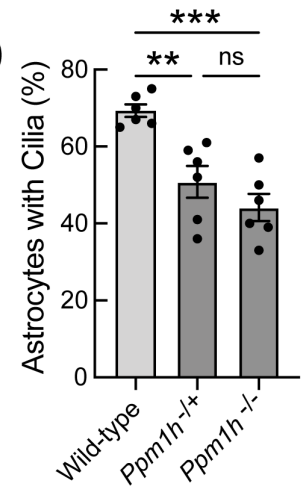
B



C



D



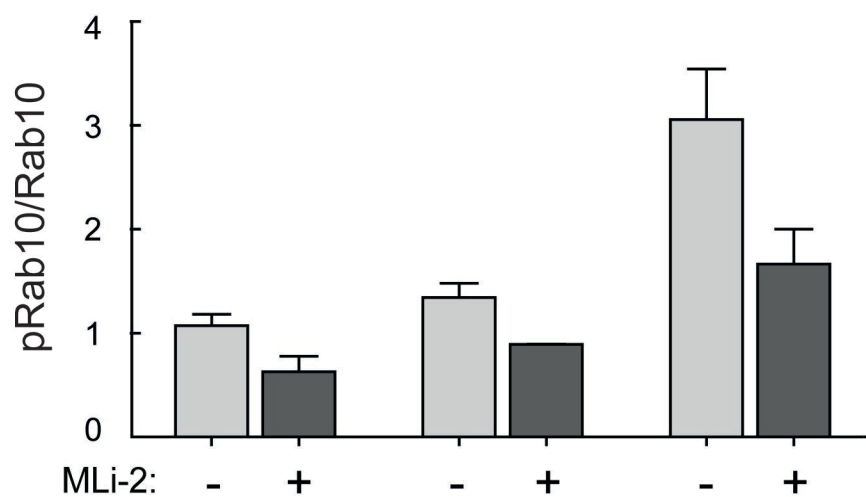
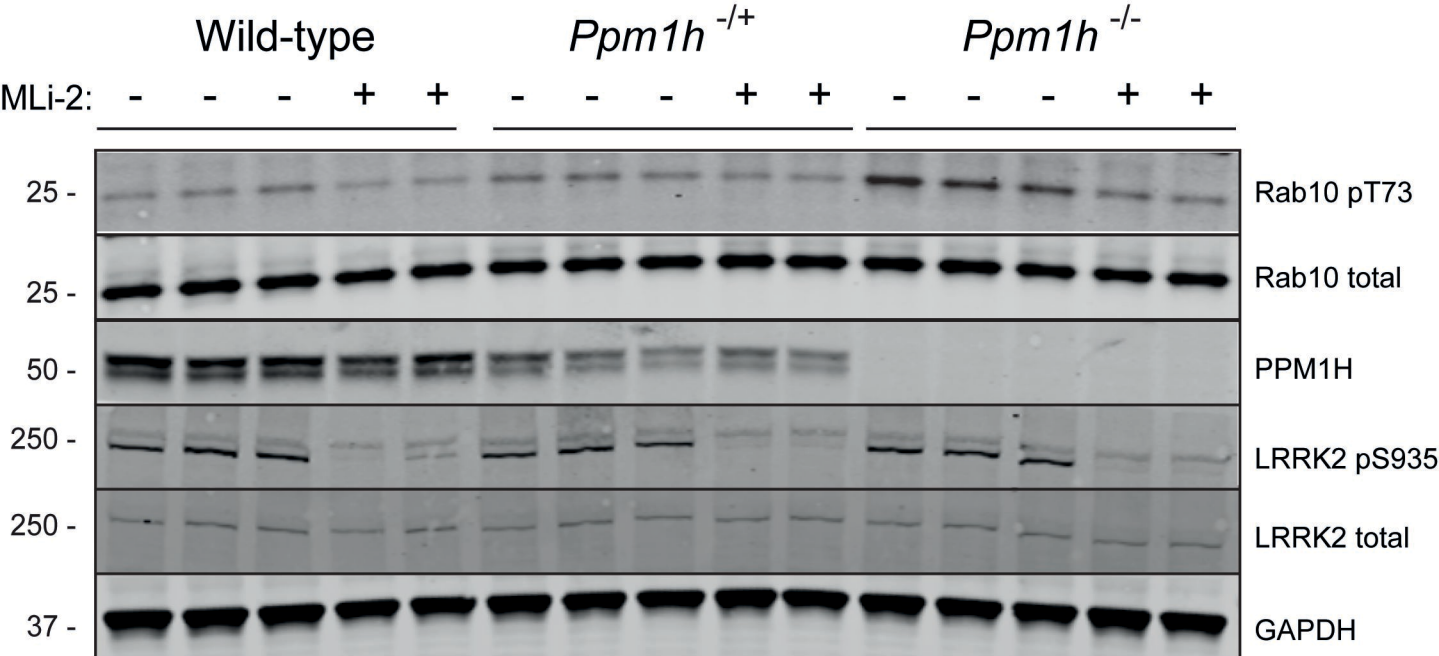
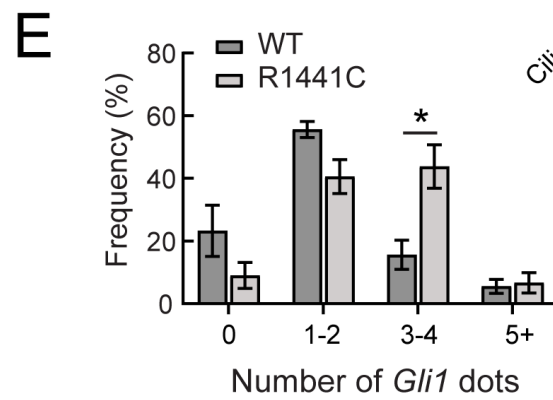
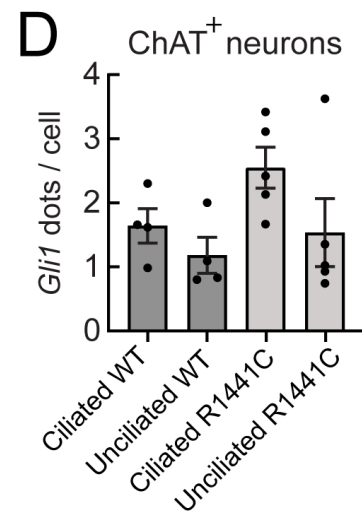
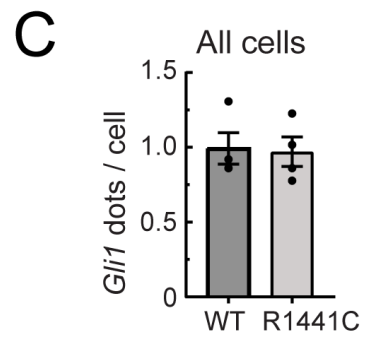
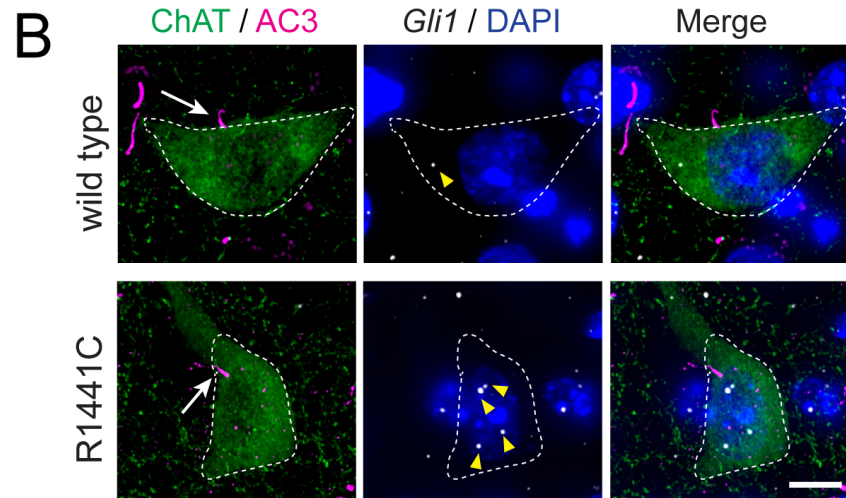
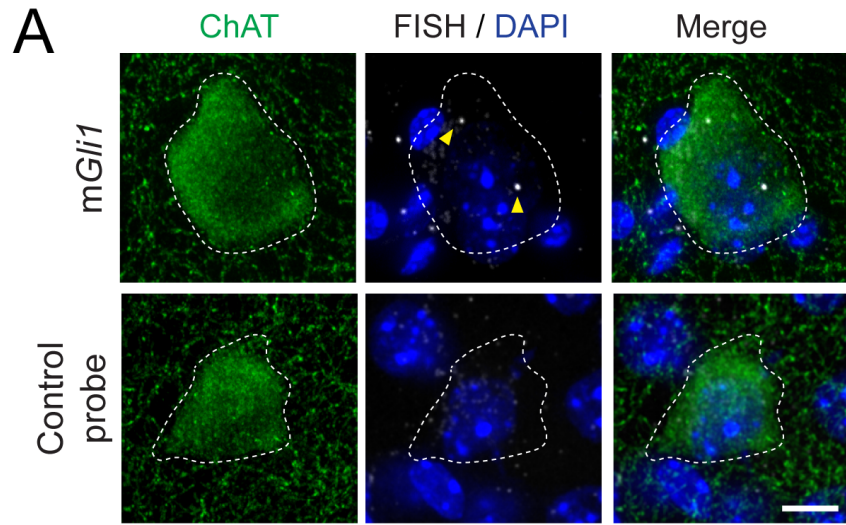
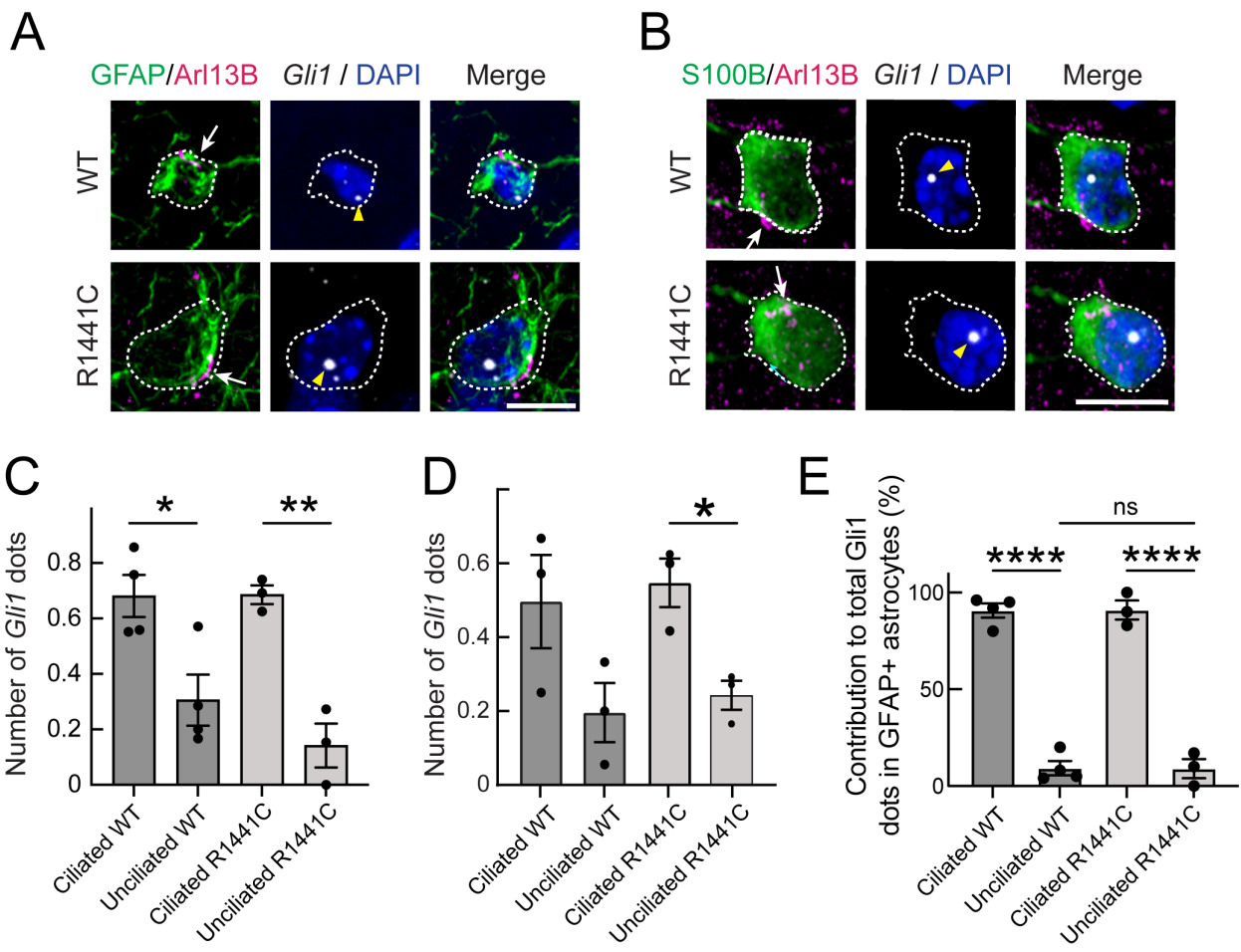
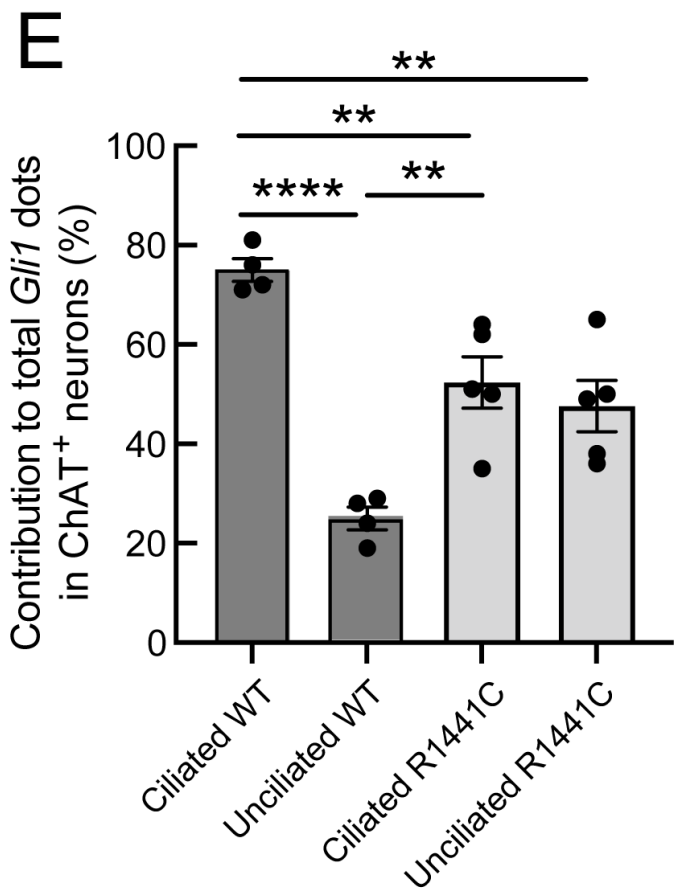
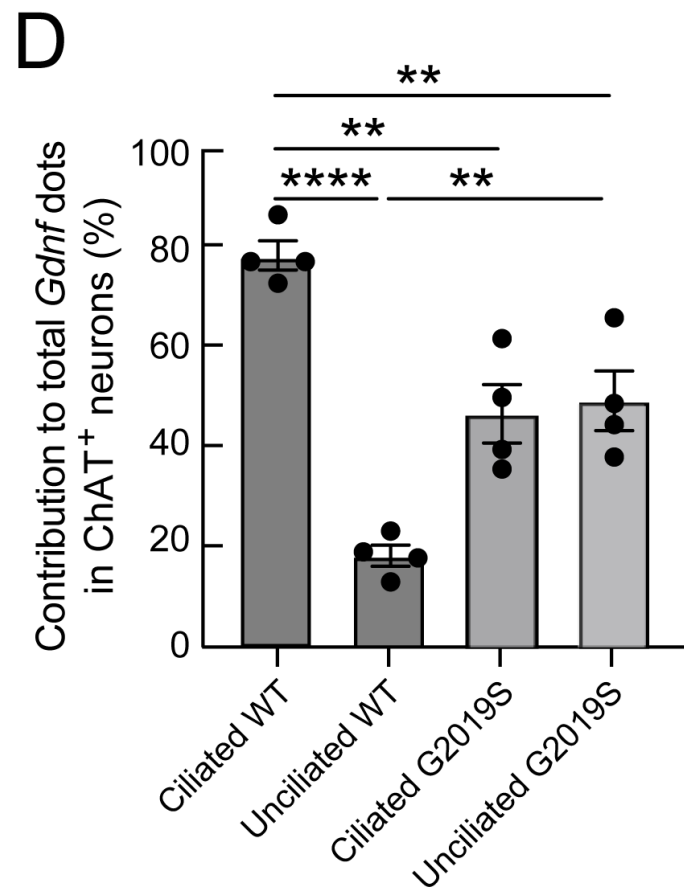
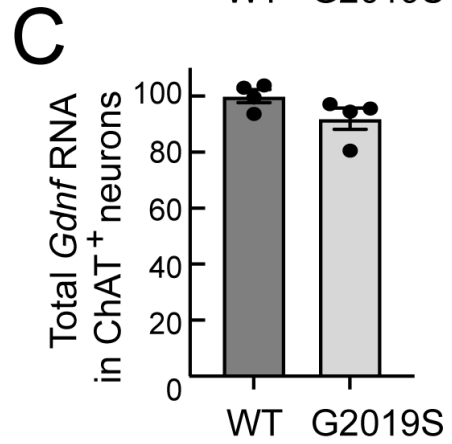
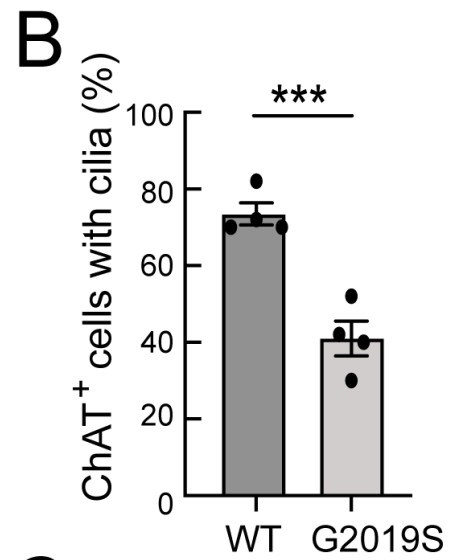
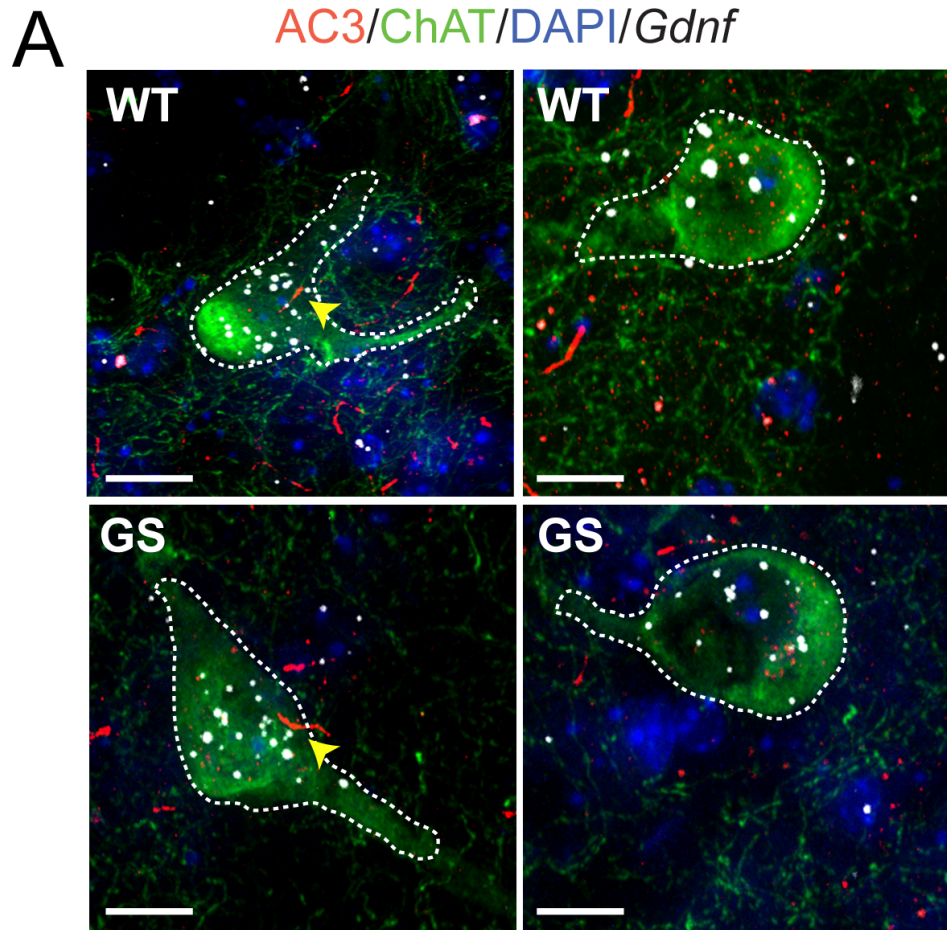


Figure 5 -- Figure Supplement 1



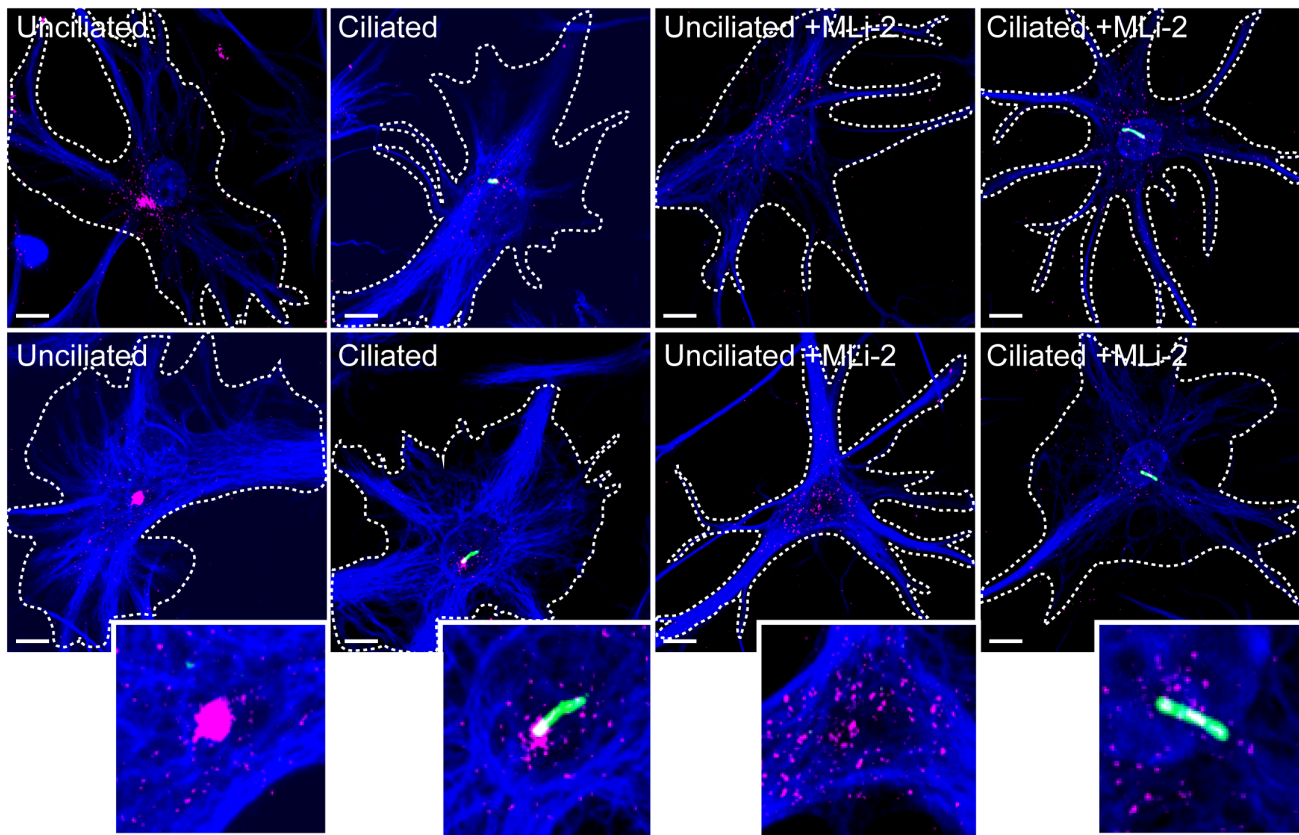


Khan et al. Fig.7

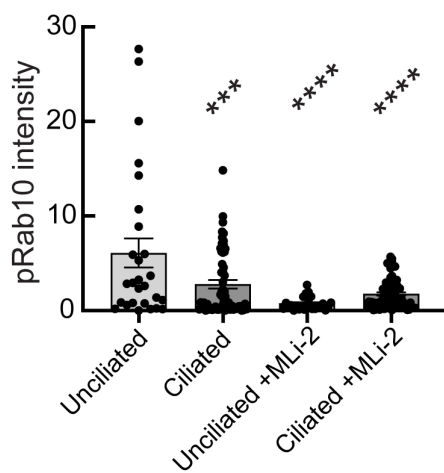


A

Arl13b/GFAP/DAPI/pRab10



B



Khan et al., Fig. 9